Modeling the plastic deformation of crystals with thin precipitates

Chung-Souk Han [a,*], June-Hyung Kim [b], Kwansoo Chung [b], Tae Jin Kang [b]

[a] *Max-Planck-Institut für Eisenforschung, Microstructure Physics and Metal Forming, Max-Planck-Str. 1, 40237 Düsseldorf, Germany*
[b] *School of Material Science and Engineering, Seoul National University, 56-1, Shinlim-Dong, Kwanak-Ku, Seoul 151-742, Korea*

Abstract

Precipitates, present in most commercial alloys, can have a strong influence on strength and hardening behavior of a single crystal. The effect of thin precipitates on the anisotropy of initial slip resistance and hardening behavior of crystals is modeled in this article. For the convenience of the computational derivation and implementation, the material formulation is given in the unrotated intermediate configuration mapped by the plastic part of the deformation gradient. Material descriptions for the considered two phased aggregates consisting in lattice hardening as well as isotropic hardening and kinematic hardening are suggested. The corresponding elastic–plastic rate-independent algorithmic treatment is derived and numerical simulations of various loading cases are presented to discuss and assess the performance of the suggested model and its rate-independent algorithmic treatment.
© 2005 Elsevier Ltd. All rights reserved.

1. Introduction

Precipitation strengthening is one of classical approaches to enhance the initial strength and hardening behavior of metals. The influences of precipitates on the mechanical characteristics of crystals and in metallic alloys have been investigated by various authors (e.g., Abel and Ham, 1966; Ashby, 1966, 1970; Brown and Stobbs, 1971b; Hosford and Zeisloft, 1972; Humphreys, 1979; Bate et al., 1981; Barlat and Vasudevan, 1991; Kiser and Zok, 1996). From these investigations, it is known that the size, shape, spacing and orientation of precipitates, which can be altered during aging processes, have strong influence on the plastic

---

* Corresponding author. Tel.: +49 2116792660; fax: +49 2116792333.
  E-mail address: han@mpie.de (C.-S. Han).

behavior. While precipitates can influence the initial yield strength and its anisotropy, they can also dominate the hardening behavior, in particular, control kinematic hardening effects (Abel and Ham, 1966). Several mechanical models related to these hardening effects have been suggested in the literature, e.g., by Tanaka and Mori (1970), Brown (1973), Hosford and Zeisloft (1972), Bate et al. (1981), Schmitt et al. (1997) and recently by Barlat and Liu (1998) for Al–Cu alloys containing θ' (Al$_2$Cu) precipitates with a volume fraction of 2–3%. This model (Barlat and Liu, 1998) is based on the elastic inclusion model (Bate et al., 1981).

Therein (Barlat and Liu, 1998) the evolution of the size of the anisotropic yield surface is described with the isotropic hardening while its macroscopic translation via kinematic hardening is formulated according to the initial structure of the precipitates of the alloy. While the influence of size of second phase particles on the flow stress is well known, the effect of the precipitates on the plastic anisotropy at the initial and deformed state has not been thoroughly investigated. Zhu et al. (2000), e.g., have shown that the orientation of platelet precipitates can have significant influences on the anisotropy of the initial yield strength in single crystals. With the influence precipitates have on single crystals, corresponding effects on the anisotropy of widely applied polycrystalline materials with precipitates can be expected. In this context, it is desirable to establish an elaborate model which can represent the effect of precipitates on the plastic anisotropy of initial yield strength as well as the isotropic hardening and kinematic hardening on single crystals.

To account for the anisotropic kinematic hardening induced by precipitates in single crystals, a crystalline elastic–plastic mechanical setting was suggested by Han et al. (2004a) and the corresponding elastic–plastic, rate-independent algorithmic treatment was derived and numerical simulations were performed by Han et al. (2004b). In this paper, the effect of thin precipitates on the anisotropy of the initial slip resistance, the isotropic hardening and the kinematic hardening is modeled and numerical simulations are performed. The material formulation is carried out in the unrotated intermediate configuration mapped by the plastic part of the deformation gradient for the convenience of the computational derivation and implementation. Various numerical procedures for single and polycrystals can be found in the literature. Depending on the considered material models, corresponding algorithmic treatments have been suggested, e.g., by Pierce et al. (1983), Cuitino and Ortiz (1992), Kalidindi and Anand (1992), Beaudoin et al. (1994), Miehe and Schröder (2001) and Clayton and McDowell (2003). By Nouailhas and Cailletaud (1995), the kinematic hardening was included to describe the behavior of single-crystal supper-alloys.

For clarity of notations, the constitutive setting in the unrotated intermediate configuration is briefly summarized in Section 2. Then, in Section 3, several descriptions for the evolution equations of the lattice hardening including the isotropic hardening and kinematic hardening induced by precipitates are suggested and discussed. The algorithmic treatment is derived relating stress, strain and internal variables increments to the convective Oldroyd derivative, in Section 4. Finally in Section 5, the evolution of the flow stress of single crystals is simulated in various crystalline orientations for different loading cases to discuss the anisotropic hardening behavior of the suggested approach.

2. Notations and constitutive setting

Kinematic relations, stress/strain-expressions and governing relations in the intermediate configuration $\widetilde{B}$ in the conventional crystal plasticity are summarized in the Table 1. Therein, the decomposition (1) of deformation gradient $\mathbf{F}$ into elastic $\mathbf{F}_e$ and plastic part $\mathbf{F}_p$ is applied, where it is assumed that the rotation of the lattice is contained in $\mathbf{F}_e$ (see Fig. 1). The plastic velocity gradient can be expressed with (4), where $\dot{\gamma}^\alpha$ denotes the plastic shearing rate, $\tilde{\mathbf{s}}^\alpha$ the slip direction and $\widetilde{\mathbf{m}}^\alpha$ the slip plane normal of slip system α in $\widetilde{B}$ with $|\tilde{\mathbf{s}}^\alpha| = |\widetilde{\mathbf{m}}^\alpha| = 1$ and $\tilde{\mathbf{s}}^\alpha \cdot \widetilde{\mathbf{m}}^\alpha = 0$.

The stress power per initial unit volume is given by $W = \mathbf{S} \cdot \dot{\mathbf{E}} = \boldsymbol{\tau} \cdot \mathbf{d}$, where $\mathbf{S}$ is the second Piola–Kirchhoff tensor in B_0 and $\boldsymbol{\tau}$ the Kirchhoff stress tensor in B. The corresponding strain terms are defined

Table 1
Kinematic relations, stress/strain expressions and governing relations in the intermediate configuration $\widetilde{B}$ in crystal plasticity

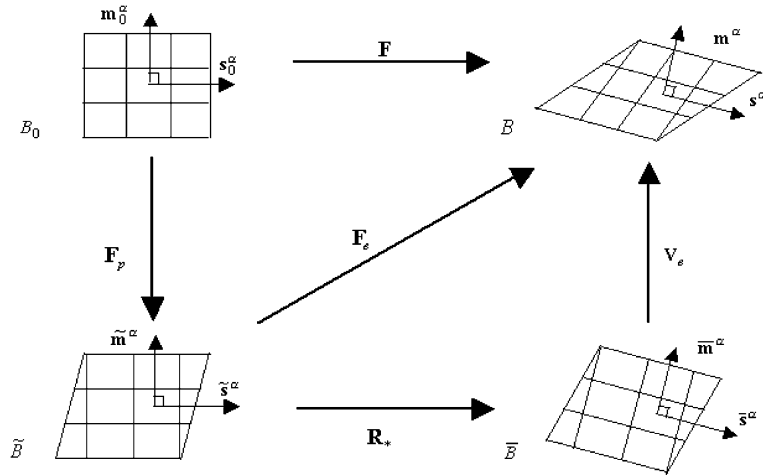|	
Multiplicative decomposition: $\mathbf{F} = \mathbf{F}_e \mathbf{F}_p$	(1)
Velocity gradient: $\mathbf{l} = \mathbf{l}_e + \mathbf{F}_e \widetilde{\mathbf{L}}_p \mathbf{F}_e^{-1}$	(2)
with $\mathbf{l}_e = \dot{\mathbf{F}}_e \mathbf{F}_e^{-1}$ and $\widetilde{\mathbf{L}}_p = \dot{\mathbf{F}}_p \mathbf{F}_p^{-1}$	(3)
Plastic velocity gradient: $\widetilde{\mathbf{L}}_p = \sum_\alpha \dot{\gamma}^\alpha (\widetilde{\mathbf{s}}^\alpha \otimes \widetilde{\mathbf{m}}^\alpha) = \widetilde{\mathbf{D}}_p + \widetilde{\mathbf{W}}_p$	(4)
$\widetilde{\mathbf{D}}_p = \sum_\alpha \dot{\gamma}^\alpha (\widetilde{\mathbf{s}}^\alpha \otimes \widetilde{\mathbf{m}}^\alpha)_s, \quad (.)_s = \frac{1}{2}[(.) + (.)^{\mathrm{T}}]$	(5)
$\widetilde{\mathbf{W}}_p = \sum_\alpha \dot{\gamma}^\alpha (\widetilde{\mathbf{s}}^\alpha \otimes \widetilde{\mathbf{m}}^\alpha)_a, \quad (.)_a = \frac{1}{2}[(.) - (.)^{\mathrm{T}}]$	(6)
Lagrangian strain tensor: $\widetilde{\mathbf{E}} = \frac{1}{2}(\mathbf{F}_e^{\mathrm{T}}\mathbf{F}_e - \mathbf{F}_p^{-\mathrm{T}}\mathbf{F}_p^{-1}) = \widetilde{\mathbf{E}}_e + \widetilde{\mathbf{E}}_p$	(7)
$\widetilde{\mathbf{E}}_e = \frac{1}{2}(\mathbf{F}_e^{\mathrm{T}}\mathbf{F}_e - \mathbf{1})$	(8)
$\widetilde{\mathbf{E}}_p = \frac{1}{2}(\mathbf{1} - \mathbf{F}_p^{-\mathrm{T}}\mathbf{F}_p^{-1})$	(9)
Second Piola–Kirchhoff stress: $\widetilde{\mathbf{S}} = \mathbf{F}_e^{-1}\boldsymbol{\tau}\mathbf{F}_e^{-\mathrm{T}}$	(10)
Mandel stress: $\widetilde{\mathbf{P}} = (\mathbf{1} + 2\widetilde{\mathbf{E}}_e)\widetilde{\mathbf{S}} = \widetilde{\mathbf{C}}_e\widetilde{\mathbf{S}}$	(11)
(assumed isotropic)elastic relation : $\widetilde{\mathbf{S}} = \widetilde{\boldsymbol{\Gamma}}_e \widetilde{\mathbf{E}}_e$	(12)
Resolved shear stress: $\tau^\alpha = \widetilde{\mathbf{P}} \cdot (\widetilde{\mathbf{s}}^\alpha \otimes \widetilde{\mathbf{m}}^\alpha)_s$	(13)
Yield function: $\Phi^\alpha = |\tau^\alpha - x^\alpha| - g^\alpha$	(14)
Kuhn–Tucker-type conditions: $\mathrm{sgn}\,(\tau^\alpha - x^\alpha)\dot{\gamma}^\alpha \geqslant 0, \quad \Phi^\alpha \leqslant 0, \quad \dot{\gamma}^\alpha \Phi^\alpha = 0$	(15)

Fig. 1. Intermediate configurations obtained by $\mathbf{F} = \mathbf{F}_e\mathbf{F}_p = \mathbf{V}_e\mathbf{R}_*\mathbf{F}_p$.

with the time derivative of the Lagrangian strain tensor E and the symmetric part of the rate of deformation tensor $\mathbf{d} = (l)_s$, respectively. An expression of W in components of $\widetilde{B}$, yields $W = \widetilde{\mathbf{S}} \cdot \widetilde{\mathbf{E}}^{\widetilde{\Delta}}$ with the Oldroyd (1950) derivative for strain like variables $(\;)^{\widetilde{\Delta}}$ describing objective and covariant strain velocities in $\widetilde{B}$.

The Clausius–Duhem inequality for isothermal processes can be stated as $W - \dot{\psi} \geqslant 0$ with the stress power W and the specific free energy ψ per unit reference volume. A reduced form of this inequality can be obtained introducing the Mandel stress tensor $\widetilde{\mathbf{P}}$ $(= (\mathbf{I} + 2\widetilde{\mathbf{E}}_e)\widetilde{\mathbf{S}})$. For this an additive split is assumed $\psi = \psi_e + \psi_p$, where ψ_e is considered to be dependent on $\mathbf{F}_e$. Its time derivative is given with $\dot{\psi}_e = \frac{\partial \psi_e}{\partial \widetilde{\mathbf{E}}_e} \cdot \dot{\widetilde{\mathbf{E}}}_e$ yielding (see, e.g., Han et al., 2003), where $\widetilde{\mathbf{S}} = \frac{\partial \psi_e}{\partial \widetilde{\mathbf{E}}_e}$, the reduced form $\widetilde{\mathbf{P}} \cdot \widetilde{\mathbf{D}}_p - \dot{\psi}_p \geqslant 0$. Thereby, use was made by the identity $\widetilde{\mathbf{D}}_p = \widetilde{\mathbf{E}}_p^{\widetilde{\Delta}}$, which can be obtained applying the Oldroyd derivative for strain like terms $(.)^{\widetilde{\Delta}} = (.) + \widetilde{\mathbf{L}}_p^{\mathrm{T}}(.) + (.)\widetilde{\mathbf{L}}_p$. For small elastic strains ψ_e can be written as $\psi_e = \frac{1}{2}\widetilde{\mathbf{E}}_e \cdot \tilde{\Gamma}_e \widetilde{\mathbf{E}}_e$ with the (assumed isotropic) elastic moduli contained in $\widetilde{\Gamma}_e$. To distinguish forward and reversed straining, the yield criterion of each slip system α shall be described here by $\Phi^\alpha = |\tau^\alpha - x^\alpha| - g^\alpha \leqslant 0$ with a back stress term x^α and the slip resistance g^α describing isotropic hardening in each slip system.

With stress-like internal variables defined by x^α and g^α, the plastic part of the free energy is reformulated as $\psi_p = -\sum_\alpha x^\alpha a^\alpha + g^\alpha z^\alpha$, where a^α and z^α are the thermo-dynamically conjugated strain-like internal variables of x^α and g^α, respectively. With the yielding conditions describing a convex elastic set in stress space, the rate of shearing $\dot{\gamma}^\alpha$ can be determined by the Kuhn–Tucker-type loading conditions $\mathrm{sign}(\tau^\alpha - x^\alpha)\dot{\gamma}^\alpha \geqslant 0$, $\Phi^\alpha \leqslant 0$, $\dot{\gamma}^\alpha \Phi^\alpha = 0$. Such descriptions would correlate to the algorithmic treatments developed by Miehe and Schröder (2001). Descriptions for the slip resistance g^α and the resolved back stress x^α would complete the material formulation, which are discussed in the following sections.

3. Evolution equations for the hardening

Precipitate induced hardening is characteristic of strong Bauschinger effects, high initial strength, rapid and strong hardening. In the elastic inclusion model (Bate et al., 1981), precipitates induce only kinematic hardening, since only elastic strains are assumed within the precipitates. Thus the hardening induced by the precipitates is considered to be kinematic and reversible. The anisotropy of the initial yield strength is not reflected in this elastic inclusion model. In the plastic inclusion model (Hosford and Zeisloft, 1972), precipitates experience the same strain as the matrix and back stresses are not considered so that the anisotropy in forward and reverse loading is not reflected. The anisotropy of the initial yield is, however, quite well reflected in this model (see, Zhu et al., 2000).

From the experimental literature (e.g., Engler et al., 2001 and the references cited therein) it is known that the deformation process of precipitated crystals is more complex. The area of the matrix remote from the particle deforms similar to single phased crystals with dislocation cells at low deformation degrees transforming to microbands at higher degrees of deformation. In the vicinity of the particles, strong lattice rotations were observed resulting particularly at the interfaces of matrix and precipitate in very high dislocation densities. The precipitates themselves are subjected to rotation, bending, and even fracture (see, Bate et al., 1981; Engler et al., 2001).

For an improved description of the mechanical characteristics of the precipitates induced hardening, a more elaborated model is suggested in this work taking account of three regions in the material (see Fig. 2): (a) the matrix area where the influence of the precipitates is negligible, (b) the precipitate area characterized by a hard material and (c) the influence area Ω characterizing the transition at strain field between the precipitate and the matrix, where lattice rotations or shading effects (Humphreys and Ardakani, 1994) and high dislocation density evolve in the deformation process. Also, the following simplifications are further assumed: (i) the material contains many inclusions (i.e., precipitates) homogeneously distributed, (ii) the inclusions do not interact with each other to any appreciable extent and (iii) the matrix and the precipitate approximately have the same elastic constants.
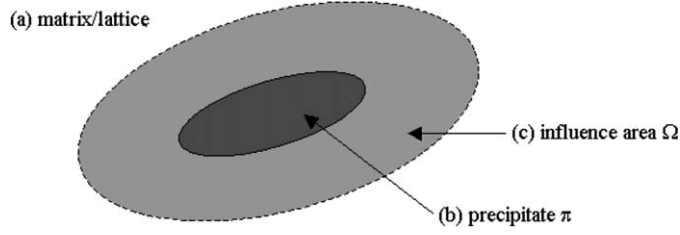
Fig. 2. Influence area Ω around a precipitate π.

In view of Fig. 2, the resolved shear stress is divided into three parts: the average resolved shear stress of the lattice τ_M^α, the average stress in the influence region τ_Ω^α weighted with the relevant area fraction ω and the average of the stress within the inclusion τ_I^α weighted with the relevant volume fraction f, yielding

$$\tau^\alpha = (1 - f - \omega)\tau_M^\alpha + \omega\tau_\Omega^\alpha + f\tau_I^\alpha. \tag{16}$$

For incorporation of such a model with the internal variable approach, the different stress components weighted with their area and volume fractions are

$$\hat{\tau}_\Omega^\alpha = \omega(\tau_\Omega^\alpha - \tau_M^\alpha) \quad \text{and} \quad \hat{\tau}_I^\alpha = f(\tau_I^\alpha - \tau_M^\alpha), \tag{17}$$

yielding

$$\tau^\alpha = \tau_M^\alpha + \hat{\tau}_\Omega^\alpha + \hat{\tau}_I^\alpha. \tag{18}$$

The influence area ω may be dependent on the size of the precipitate. For simplicity, however, it is assumed that ω is proportional to f, which yields both hardening components $\hat{\tau}_\Omega^\alpha$ and $\hat{\tau}_I^\alpha$ to be proportional to f in (17).

As correspondence to the internal variables applied in (14), it is suggested to correlate the slip resistance to the hardening mechanisms of the matrix $g^\alpha = \tau_M^\alpha + \hat{\tau}_\Omega^\alpha$ and, following Bate et al. (1981), the back stress to the stress in the precipitate, as $x^\alpha = \hat{\tau}_I^\alpha$. In average, the elastic range and thus also the back stresses are assumed to be small in Ω and negligible in the matrix area. In the following the kinematic hardening related to Ω is, as for other regions of the lattice, neglected.

3.1. Hardening of the lattice

The rate of the strain-like internal variable associated with g^α is independent of sign $(\dot{\gamma}^\alpha)$ and thus identified with the magnitude of the shear rate $|\dot{\gamma}^\alpha|$. The evolution of the slip resistance τ_M^α is usually described by the hardening law

$$\dot{\tau}_M^\alpha = \sum_\beta h_M^{\alpha\beta}|\dot{\gamma}^\beta| \tag{19}$$

with initial value τ_{Mo}^α and the work hardening moduli of the lattice $h_M^{\alpha\beta}$. A widely applied description for the work hardening moduli given as

$$h_M^{\alpha\beta} = [q_M + (1 - q_M)\delta^{\alpha\beta}]h_M^\beta, \tag{20}$$

where q_M ranges from 1.0 to 1.4 and represents the ratio of the latent hardening to the self-hardening and the single slip hardening rate h_M^β.

A more complex description was for instance suggested by Zhou et al. (1993) where, in addition to different slip systems, the relation to different slip planes was treated in specific ways. In the literature, various

forms have been also suggested for the description of h_M^β, by Anand and Kothari (1996) and Zhou et al. (1993), the self-hardening of a pure single crystal is suggested in the power-law relation as

$$h_M^\beta = \tau_M^0 \left(\frac{c_M \gamma}{b_M \tau_M^0} + 1 \right)^{b_M}, \quad \text{where } \gamma = \sum_\alpha \gamma^\alpha \left(= \sum_\alpha \int |\mathrm{d}\dot\gamma^\alpha| \, \mathrm{d}t \right). \tag{21}$$

3.2. Hardening induced by precipitates

For small to moderate strains, the precipitate is usually assumed not to be subjected to plastic strain. The averaged stress of the precipitate τ_I^α is, therefore, assumed to be reversible and reflects here the back stress term. With significant higher yield stresses in the precipitates than in the lattice, high dislocation densities can be expected in the close neighborhood of the precipitates and lattice rotation/shading around precipitates will result in additional hardening of the material. With the precipitate structure and morphology being inhomogeneous, the dislocation density distribution and lattice rotations around the precipitates can also be expected to be anisotropic and, thus, also yields anisotropic hardening. Precipitates are known to induce also higher initial values in the critical resolved shear stresses which can be explained by bowing of dislocations. The critical resolved shear stresses are again dependent on the precipitate structure/morphology.

Thin precipitates, considered here, like the θ' precipitates, are normally aligned parallel to the habit planes (see Fig. 3) after the aging process. The volume fraction of each habit plane can vary depending on the aging process. In the deformation process of the aggregate, the inhomogeneous deformation is in part accommodated (see, e.g., Hosford and Zeisloft, 1972; Bate et al., 1981; Engler et al., 2001; Han et al., 2004a) by rotations of the precipitates relative to the lattice, as indicated in Fig. 4.

3.3. Isotropic hardening induced by precipitates

In shear deformation inducing precipitate rotation, Hosford and Zeisloft (1972) assumed the hardening effect of the precipitates to be negligible. Therefore, the shear strains have been excluded in the incremental
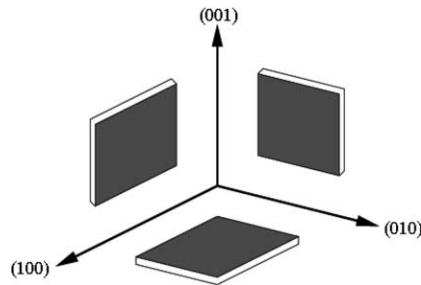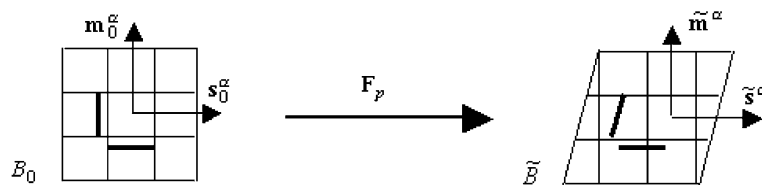

Fig. 3. Precipitates in habit planes.

Fig. 4. Rotation of precipitates by $\mathbf{F}_p$.

plastic work $d\omega_p = \bar{\tau} d\bar{\varepsilon}_p$, where $\bar{\tau}$ denotes the equivalent stress and $d\bar{\varepsilon}_p$ the equivalent plastic strain. Considering only the area Ω and single slip deformation, the neglect of these shear strains can be expressed with the increments in its related plastic potential as

$$\dot{\Psi}_p^\Omega = \frac{1}{f} \sum_\alpha \sum_\pi f^\pi s_\Omega^\pi |\dot{\gamma}^\alpha| \sqrt{(\widetilde{\mathbf{s}}^\alpha \otimes \widetilde{\mathbf{m}}^\alpha)_S \cdot \widetilde{\mathbf{H}}^\pi (\widetilde{\mathbf{s}}^\alpha \otimes \widetilde{\mathbf{m}}^\alpha)_S}, \tag{22}$$

where f^π is the volume fraction of the precipitates parallel to the habit plane π, s_Ω^π is a weight function to describe initial hardening and saturation behavior, while the fourth order tensor $\widetilde{\mathbf{H}}^\pi$ is defined as

$$\widetilde{\mathbf{H}}^\pi = \sum_{ijkl}^3 H_{ijkl}^\pi \widetilde{\mathbf{e}}_i^\pi \otimes \widetilde{\mathbf{e}}_j^\pi \otimes \widetilde{\mathbf{e}}_k^\pi \otimes \widetilde{\mathbf{e}}_l^\pi \tag{23}$$

with the base vectors of the precipitates $\widetilde{\mathbf{e}}_i^\pi$. The components of $\widetilde{\mathbf{H}}^\pi$ can be given with $H_{ijkl}^\pi = 1$ for $i = j = k = l$, $(i,j,k,l) = (2,3,2,3)$, $(i,j,k,l) = (3,2,3,2)$ and otherwise $H_{ijkl}^\pi = 0$ for a platelet precipitate aligned to $[1\,0\,0]$ plane and $\widetilde{\mathbf{e}}_i^\pi$ parallel to $(1\,0\,0)$, $(0\,1\,0)$, and $(0\,0\,1)$, respectively. The expressions for $\widetilde{\mathbf{H}}^\pi$ aligned to other habit planes are then obtained by rotation of $\widetilde{\mathbf{e}}_i^\pi$, $i = 1, 2, 3$. The reorientation of precipitates is described by $\widetilde{\mathbf{e}}_t^\pi = \frac{\mathbf{F}_p \widetilde{\mathbf{e}}_{t0}^\pi}{|\mathbf{F}_p \widetilde{\mathbf{e}}_{t0}^\pi|}$ for precipitate orientation vectors in the tangential plane of the disc, therefore, by $\widetilde{\mathbf{e}}_n^\pi = \frac{\mathbf{F}_p^{-T} \widetilde{\mathbf{e}}_{n0}^\pi}{|\mathbf{F}_p^{-T} \widetilde{\mathbf{e}}_{n0}^\pi|}$ for the unit normal vector.

With $h_\Omega^\pi = \frac{\partial s_\Omega^\pi}{\partial \gamma^\alpha}$, the increments of the corresponding resolved shear terms can be given approximately as

$$\dot{\hat{\tau}}_\Omega^\alpha = \frac{1}{f} \sum_\pi f^\pi h_\Omega^{\pi\alpha} |\dot{\gamma}^\alpha| \sqrt{(\widetilde{\mathbf{s}}^\alpha \otimes \widetilde{\mathbf{m}}^\alpha)_S \cdot \widetilde{\mathbf{H}}^\pi (\widetilde{\mathbf{s}}^\alpha \otimes \widetilde{\mathbf{m}}^\alpha)_S} \tag{24}$$

for slip system α by neglecting dependencies of $\widetilde{\mathbf{H}}^\pi$ on $\dot{\gamma}^\alpha$. For the functions $h_\Omega^{\pi\alpha}$, the self-hardening descriptions suggested by Chang and Asaro (1981) can be used, i.e.,

$$h_\Omega^{\pi\alpha} = h_\Omega^o \,\mathrm{sech}^2\left(\frac{h_\Omega^o \gamma}{\tau_\Omega^S - \tau_\Omega^o}\right) \tag{25}$$

with material parameters h_Ω^o, τ_Ω^S and τ_Ω^o. The description in (24) for a single slip does not reflect latent hardening. The generalization of this description to the multiple slip deformation incorporating the latent hardening is suggested as

$$\dot{\hat{\tau}}_\Omega^\alpha = \sum_\beta h_\Omega^{\alpha\beta} |\dot{\gamma}^\beta|, \tag{26}$$

where

$$h_\Omega^{\alpha\beta} = [q_\Omega + (1 - q_\Omega)\delta^{\alpha\beta}] h_\Omega^\beta \quad \text{with } h_\Omega^\alpha = \frac{1}{f} \sum_\pi f^\pi h_\Omega^{\pi\alpha} \sqrt{(\widetilde{\mathbf{s}}^\alpha \otimes \widetilde{\mathbf{m}}^\alpha)_S \cdot \widetilde{\mathbf{H}}^\pi (\widetilde{\mathbf{s}}^\alpha \otimes \widetilde{\mathbf{m}}^\alpha)_S}. \tag{27}$$

Initial values are given as

$$\hat{\tau}_{\Omega o}^\alpha = \frac{1}{f} \sum_\pi f^\pi s_{\Omega o}^\pi \sqrt{(\widetilde{\mathbf{s}}^\alpha \otimes \widetilde{\mathbf{m}}^\alpha)_S \cdot \widetilde{\mathbf{H}}^\pi (\widetilde{\mathbf{s}}^\alpha \otimes \widetilde{\mathbf{m}}^\alpha)_S}, \tag{28}$$

where $s_{\Omega o}^\pi$ is a material parameter which influences the initial anisotropy in the yield stress.

3.4. Kinematic hardening induced by precipitates

If the back stress is related to averaged stresses in the precipitates and the deformation of the precipitate is assumed to be elastic, then $\hat{\tau}_I = \mathbf{\Gamma}_e \hat{\varepsilon}_I$. Now to project the internal strain from the overall strain of the

aggregate, Bate et al. (1981) and Brown and Stobbs (1971a,b) proposed the elastic inclusion model, as suggested by Han et al. (2004a) in a crystalline setting, in which $\varepsilon_e^I = K\varepsilon_p$, is derived modifying the Eshelby formalism for elasticity to elasto-plasticity with the accommodation tensor $\mathbf{K} = \mathbf{I} - \langle \mathbf{\Lambda} \rangle$. While the Eshelby formalism is exact for elasticity, for elasto-plasticity such an approach can only be seen as an approximation. In general, other operators than $\mathbf{K}$ projecting the internal strains from the overall strain of the aggregate could also be applied. Assuming again that the hardening of shear deformation inducing precipitate rotation is negligible another possibility is to use $\widetilde{\mathbf{H}}^{\pi}$ as a projection operator for simplicity. This would yield

Table 2
Hardening descriptions for a single crystal with thin precipitates

Slip resistance

$$\dot{g}^{\alpha} = \sum_{\beta}(h_M^{\alpha\beta} + h_{\Omega}^{\alpha\beta})|\dot{\gamma}^{\beta}|$$

With work hardening moduli of the lattice

$$h_M^{\alpha\beta} = [q_M + (1 - q_M)\delta^{\alpha\beta}]h_M^{\beta}$$

$$h_M^{\beta} = \tau_M^0 \left(\frac{c_M \gamma}{b_M \tau_M^0} + 1 \right)^{b_M}$$

And the moduli related to the hardening induced by precipitates

$$h_{\Omega}^{\alpha\beta} = [q_M + (1 - q_M)\delta^{\alpha\beta}]h_{\Omega}^{\beta}$$

$$h_{\Omega}^{\alpha} = \frac{1}{f}\sum_{\pi}f^{\pi}h_{\Omega}^{\pi^{\alpha}}\sqrt{(\tilde{\mathbf{s}}^{\alpha} \otimes \tilde{\mathbf{m}}^{\alpha})_S \cdot \widetilde{\mathbf{H}}^{\pi}(\tilde{\mathbf{s}}^{\alpha} \otimes \tilde{\mathbf{m}}^{\alpha})_S}$$

$$h_{\Omega}^{\pi^{\alpha}} = h_{\Omega}^o \operatorname{sech}^2\left(\frac{h_{\Omega}^o \gamma}{\tau_{\Omega}^S - \tau_{\Omega}^o} \right)$$

$$\widetilde{\mathbf{H}}^{\pi} = \sum_{ijkl}^{3} H_{ijkl}^{\pi}\tilde{\mathbf{e}}_i^{\pi} \otimes \tilde{\mathbf{e}}_j^{\pi} \otimes \tilde{\mathbf{e}}_k^{\pi} \otimes \tilde{\mathbf{e}}_l^{\pi}$$

Kinematic hardening induced by precipitates

$$\hat{\tau}_I^{\alpha} = x^{\alpha} = \widetilde{\mathbf{C}}_e\widetilde{\mathbf{X}} \cdot (\tilde{\mathbf{s}}^{\alpha} \otimes \tilde{\mathbf{m}}^{\alpha})_S$$

With

$$\widetilde{\mathbf{X}}^{\widetilde{\nabla}} = c_x f \widetilde{\mathbf{\Gamma}}_e \widetilde{\mathbf{H}} \sum_{\beta}\dot{\gamma}^{\beta}(\tilde{\mathbf{s}}^{\beta} \otimes \tilde{\mathbf{m}}^{\beta})_S - b_x|\dot{\gamma}|\widetilde{\mathbf{X}} \quad \text{and} \quad \widetilde{\mathbf{H}} = \frac{1}{f}\sum_{\pi}f^{\pi}\widetilde{\mathbf{H}}^{\pi}$$

$$\hat{\tau}_I^\alpha = \frac{1}{f} \sum_\pi f^\pi x^{\pi^\alpha},$$ (29)

where

$$x^{\pi^\alpha} = \widetilde{\mathbf{C}}_e \widetilde{\mathbf{X}}^\pi \cdot (\tilde{\mathbf{s}}^\alpha \otimes \widetilde{\mathbf{m}}^\alpha)_S \quad \text{with} \quad \widetilde{\mathbf{X}}^{\pi^{\overset{\nabla}{}}} = c_x f \widetilde{\mathbf{\Gamma}}_e \widetilde{\mathbf{H}}^\pi \sum_\beta \dot{\gamma}^\beta (\tilde{\mathbf{s}}^\beta \otimes \widetilde{\mathbf{m}}^\beta)_S - b_x |\dot{\gamma}| \widetilde{\mathbf{X}}^\pi.$$ (30)

Here, $\dot{\gamma} = \sum_\alpha \dot{\gamma}^\alpha$ and $\widetilde{\mathbf{C}}_e = \mathbf{1} + 2\widetilde{\mathbf{E}}_e = \mathbf{F}_e^T \mathbf{F}_e$ as a right Cauchy–Green tensor, while b_x and c_x are material constants, and $(.)^{\overset{\nabla}{}}$ is the Oldroyd derivative for stress like terms given with $(.)^{\overset{\nabla}{}} = (.)^{\cdot} - \widetilde{\mathbf{L}}_p( ) - ( )\widetilde{\mathbf{L}}_p^T$ which is identical to the Lie derivative (see, e.g., Cuitino and Ortiz, 1992; Han et al., 2003). Note that in rate description of the back stress in (30) incorporates saturation behavior observed in experiments usually related to relaxation mechanisms like dislocation annihilation and cross slip. By combining all back stress tensors $\widetilde{\mathbf{X}}^\pi$ of each precipitate π for a single back stress tensor $\widetilde{\mathbf{X}}$, this formulation can be simplified to

$$\hat{\tau}_I^\alpha = x^\alpha = \widetilde{\mathbf{C}}_e \widetilde{\mathbf{X}} \cdot (\tilde{\mathbf{s}}^\alpha \otimes \widetilde{\mathbf{m}}^\alpha)_S,$$ (31)

where

$$\widetilde{\mathbf{X}}^{\overset{\nabla}{}} = c_x f \widetilde{\mathbf{\Gamma}}^e \widetilde{\mathbf{H}} \sum_\beta \dot{\gamma}^\beta (\tilde{\mathbf{s}}^\beta \otimes \widetilde{\mathbf{m}}^\beta)_S - b_x |\dot{\gamma}| \widetilde{\mathbf{X}} \quad \text{with} \quad \widetilde{\mathbf{H}} = \frac{1}{f} \sum_\pi f^\pi \widetilde{\mathbf{H}}^\pi$$ (32)

and $\widetilde{\mathbf{X}}$ is assumed to vanish initially.

Although it is well known, it should be noted that the fine-to-small particles give the highest strengthening and hardening effects. For example, a small volume fraction of fine precipitates can increase the yield strength of pure aluminum by 20 times, while the increase of the yield strength with large precipitates is generally less effective. Besides, the particle size effect becomes much more drastic as the particle diameter decreases. This size effect is not reflected by the suggested model and material parameters have to be adjusted. Such size effects could be modeled by size dependent strain gradient material descriptions (see, e.g., Shu, 1998; Meissonnier et al., 2001; Kim and Oh, 2003; Evers et al., 2002, 2004; Ohashi, 2004; Han et al., 2005a,b) and an explicit discretization of the precipitate structure. This however would be computationally quite costly and not applicable for large scale aggregates or poly-crystals. All hardening descriptions of the suggested material model are summarized in Table 2. The algorithmic treatment for the evolution equations of the hardening descriptions follows in the next section.

4. Numerical algorithm

As a starting point, all variables at the time step t_n are assumed to be known and the current time shall be given with t_{n+1}. In what follows, however, all variables without subscript are evaluated at time t_{n+1}. With $\widetilde{\mathbf{S}}$ dependent on the elastic strain or stretch tensors; i.e., $\widetilde{\mathbf{C}}_e$, these tensors have to be updated from t_n to t_{n+1}. The plastic deformation gradient can be written as $\mathbf{F}_p = \exp(\Delta t \widetilde{\mathbf{L}}_p) \mathbf{F}_p^n$, which is approximated here by $\mathbf{F}_p \approx (\mathbf{1} + \Delta t \widetilde{\mathbf{L}}_p) \mathbf{F}_p^n = (\mathbf{1} + \sum_\alpha \Delta \gamma^\alpha \tilde{\mathbf{s}}^\alpha \otimes \widetilde{\mathbf{m}}^\alpha) \mathbf{F}_p^n$ where $\mathbf{1}$ is the identity tensor. Assuming no plastic deformation, the trial value for the elastic deformation gradient is obtained as $\mathbf{F}_e^{\text{trial}} = \mathbf{F}(\mathbf{F}_p^n)^{-1}$, yielding the elastic right Cauchy–Green tensor $\widetilde{\mathbf{C}}_e = \mathbf{F}_e^T \mathbf{F}_e$. After $\Delta \gamma^\alpha$ are iteratively obtained as discussed later, the updated strain can be written as (see, e.g., Kalidindi and Anand, 1992; Cuitino and Ortiz, 1992)

$$\widetilde{\mathbf{C}}_e = \widetilde{\mathbf{C}}_e^{\text{trial}} - 2\left(\widetilde{\mathbf{C}}_e^{\text{trial}} \sum_\alpha \Delta \gamma^\alpha \tilde{\mathbf{s}}^\alpha \otimes \widetilde{\mathbf{m}}^\alpha \right)_s + O(\Delta \gamma^{\alpha 2}), \quad \text{where} \quad \widetilde{\mathbf{C}}_e^{\text{trial}} = \mathbf{F}_e^{\text{trial}T} \mathbf{F}_e^{\text{trial}}.$$ (33)

With the trial stresses $\widetilde{\mathbf{S}}^{\text{trial}} = \widetilde{\boldsymbol{\Gamma}}_e \frac{1}{2}(\widetilde{\mathbf{C}}_e^{\text{trial}} - \mathbf{1})$ and neglecting quadratic and higher terms in $\Delta\gamma^\alpha$ the updated stress is obtained as

$$\widetilde{\mathbf{S}} = \widetilde{\mathbf{S}}^{\text{trial}} - \widetilde{\boldsymbol{\Gamma}}_e \left(\widetilde{\mathbf{C}}_e^{\text{trial}} \sum_\alpha \Delta\gamma^\alpha \widetilde{\mathbf{s}}^\alpha \otimes \widetilde{\mathbf{m}}^\alpha \right)_s. \tag{34}$$

The Kirchhoff stress can then be computed via $\boldsymbol{\tau} = \mathbf{F}_e \widetilde{\mathbf{S}} \mathbf{F}_e^{\text{T}}$, where $\mathbf{F}_e = \mathbf{F}(\mathbf{F}_p^{n+1})^{-1}$.

For the numerical treatment of the back stress, the evolution equations in stress-like internal variables $\widetilde{\mathbf{X}}^{\widetilde{\nabla}} = c_x f \widetilde{\boldsymbol{\Gamma}}_e \widetilde{\mathbf{H}} \sum_\alpha \dot{\gamma}^\alpha (\widetilde{\mathbf{s}}^\alpha \otimes \widetilde{\mathbf{m}}^\alpha)_S - b_x |\dot{\gamma}| \widetilde{\mathbf{X}}$ are considered. Applying the Oldroyd derivative, an incremental form for the back stresses evolution can be given with $\widetilde{\mathbf{X}}^{\widetilde{\nabla}} = \dot{\widetilde{\mathbf{X}}} - \widetilde{\mathbf{L}}_p \widetilde{\mathbf{X}} - \widetilde{\mathbf{X}} \widetilde{L}_p^{\text{T}}$, $\widetilde{\mathbf{X}} = \mathbf{f}_p \widetilde{\mathbf{X}}^n \mathbf{f}_p^{\text{T}} + \Delta \widetilde{\mathbf{X}}^{\widetilde{\nabla}}$ where $\mathbf{f}_p$ is the plastic incremental deformation gradient; i.e., $\mathbf{f}_p = \mathbf{F}_p \mathbf{F}_p^{n^{-1}} = \mathbf{1} + \Delta t \widetilde{\mathbf{L}}_p$ and the increments in the back stresses are written as $\Delta \widetilde{\mathbf{X}}^{\widetilde{\nabla}} = c_x f \widetilde{\boldsymbol{\Gamma}}_e \widetilde{\mathbf{H}} \sum_\alpha \Delta\gamma^\alpha (\widetilde{\mathbf{s}}^\alpha \otimes \widetilde{\mathbf{m}}^\alpha)_S - b_x |\Delta\gamma| \widetilde{\mathbf{X}}$ with $\Delta\gamma = \sum_{\alpha \in A} |\Delta\gamma^\alpha|$, yielding

$$\widetilde{\mathbf{X}} = \frac{1}{1 + b_x |\Delta\gamma|} \left(\mathbf{f}_p \widetilde{\mathbf{X}}^n \mathbf{f}_p + c_x f \widetilde{\boldsymbol{\Gamma}}_e \widetilde{\mathbf{H}} \sum_\alpha \Delta\gamma^\alpha (\widetilde{\mathbf{s}}^\alpha \otimes \widetilde{\mathbf{m}}^\alpha)_S \right). \tag{35}$$

With (13 and 31), the trial resolved shear stress and back stress terms on each slip system α are given by $\tau^{\alpha\text{trial}} = \widetilde{\mathbf{C}}_e^{\text{trial}} \widetilde{\mathbf{S}}^{\text{trial}} \cdot (\widetilde{\mathbf{s}}^\alpha \otimes \widetilde{\mathbf{m}}^\alpha)_s$ and $x^{\alpha\text{trial}} = \widetilde{\mathbf{C}}_e^{\text{trial}} \widetilde{\mathbf{X}}^{\text{trial}} \cdot (\widetilde{\mathbf{s}}^\alpha \otimes \widetilde{\mathbf{m}}^\alpha)_s$, respectively. If the elastic strains are assumed to be infinitesimal, as commonly assumed for metallic materials, $\widetilde{\mathbf{C}}_e$ can be neglected in the determination of the resolved terms, yielding $\tau^{\alpha\text{trial}} = \widetilde{\mathbf{S}}^{\text{trial}} \cdot (\widetilde{\mathbf{s}}^\alpha \otimes \widetilde{\mathbf{m}}^\alpha)_s$ and $x^{\alpha\text{trial}} = x^{\alpha^n} = \widetilde{\mathbf{X}}^n \cdot (\widetilde{\mathbf{s}}^\alpha \otimes \widetilde{\mathbf{m}}^\alpha)_s$, which is applied here. For the time step $n + 1$ satisfying

$$\Phi^{\alpha\text{trial}} = |\tau^{\alpha\text{trial}} - x^{\alpha\text{trial}}| - g^{\alpha^n} \leqslant 0, \quad \forall\alpha \in S, \tag{36}$$

the time step $n + 1$ is elastic. If (36) is violated for a slip system $\alpha \in S$, the step is elasto-plastic. Here, $S = \{1, \ldots, m\}$ denotes the set of possible slip systems of the single crystal.

If the flow criterion is violated by $\Phi^{\alpha\text{trial}} > 0$ for some $\alpha \in S$, the plastic consistency conditions have to be satisfied by variation of $\Delta\gamma^\alpha$. The main problem now is that the set of active slip systems

$$A = \{\alpha \in S | \text{sign}(\tau^\alpha - x^\alpha)\Delta\gamma^\alpha \geqslant 0 \text{ and } \Phi^\alpha \geqslant 0\} \tag{37}$$

at the end of the time interval is not known a priori and not uniquely determined by the trial state.

Therefore, an iterative active set search procedure is performed, which is discussed in more detail in Han et al. (2004b) and has been summarized in Appendix A. In the following, it is assumed that the active set of slip systems A is given. Then, for all $\alpha \in A$ the actual incremental parameters $\Delta\gamma^\alpha$ are determined from the associated consistency conditions.

4.1. Determination of plastic slip at a given active slip system set

Based on the representation of the stresses (34) and the back stresses (35), the consistency conditions can be recast in the form

$$r^\alpha = \Phi^\alpha = \text{sign}(\tau^\alpha - x^\alpha)(\tau^\alpha - x^\alpha) - g^\alpha = 0, \quad \alpha \in A. \tag{38}$$

The solution of this condition for the plastic parameters $\Delta\gamma^\alpha$ is performed by a local Newton iteration based on the linearization of (38)

$$r^{\alpha^k} - \sum_{\beta \in A} D^{\alpha\beta^k} \Delta\Delta\gamma^{\beta^{k+1}} = 0, \quad \forall\alpha \in A \tag{39}$$

with the iteration index k, the Jacobian matrix $D^{\alpha\beta^k} = -\frac{\partial r^\alpha}{\partial \Delta\gamma^\beta}$ and $\Delta\gamma^{\alpha^{k+1}} = \Delta\gamma^{\alpha^k} + \Delta\Delta\gamma^{\alpha^{k+1}}$.

With $r^\alpha = \text{sign}(\Delta\gamma^\alpha)(\tau^\alpha - x^\alpha) - g^\alpha$, the components of the Jacobian matrix are obtained as

$$D^{\alpha\beta} = -\frac{\partial r^\alpha}{\partial \Delta\gamma^\beta} = -\text{sign}(\Delta\gamma^\alpha)\left(\frac{\partial \tau^\alpha}{\partial \Delta\gamma^\beta} - \frac{\partial x^\alpha}{\partial \Delta\gamma^\beta}\right) + \frac{\partial g^\alpha}{\partial \Delta\gamma^\beta} \tag{40}$$

The iteration is repeated until a convergence criterion is fulfilled, i.e., $|\mathbf{r}| = \sqrt{\sum_{\alpha\in A}(r^\alpha)^2} \leqslant \text{tol}$. With $\Delta\gamma^\alpha$ determined by the Newton iteration, all needed variables can be updated for a given active set A. Now, the determination of the components $\frac{\partial \tau^\alpha}{\partial \Delta\gamma^\beta}$, $\frac{\partial x^\alpha}{\partial \Delta\gamma^\beta}$ and $\frac{\partial g^\alpha}{\partial \Delta\gamma^\beta}$ needed for the evaluation of (40) follows.

The dependence for the resolved shear stress with respect to $\Delta\gamma^\alpha$, $\alpha \in A$ can be given as
$\tau^\alpha = \tau^{\alpha^{\text{trial}}} - (\widetilde{\mathbf{s}}^\alpha \otimes \widetilde{\mathbf{m}}^\alpha)_s \cdot \widetilde{\boldsymbol{\Gamma}}_e\left(\widetilde{\mathbf{C}}_e^{\text{trial}}\sum_\beta \Delta\gamma^\beta \widetilde{\mathbf{s}}^\beta \otimes \widetilde{\mathbf{m}}^\beta\right)_s$ yielding the derivation

$$\frac{\partial \tau^\alpha}{\partial \Delta\gamma^\beta} = -(\widetilde{\mathbf{s}}^\alpha \otimes \widetilde{\mathbf{m}}^\alpha)_s \cdot \widetilde{\boldsymbol{\Gamma}}_e(\widetilde{\mathbf{C}}_e^{\text{trial}}\widetilde{\mathbf{s}}^\beta \otimes \widetilde{\mathbf{m}}^\beta)_s. \tag{41}$$

With $g^\alpha = g^{\alpha^n} + \Delta g^\alpha$ and evolution equation $\dot{g}^\alpha = \sum_\beta(h_M^{\alpha\beta} + h_\Omega^{\alpha\beta})|\dot{\gamma}^\beta|$, $\Delta g^\alpha = \sum_\beta(h_M^{\alpha\beta} + h_\Omega^{\alpha\beta})|\Delta\gamma^\beta|$ is obtained, which yields the derivation as

$$\frac{\partial g^\alpha}{\partial \Delta\gamma^\beta} = \sum_\delta \left\{[q_M + (1 - q_M)\delta^{\alpha\delta}]\left[\text{sign}(\Delta\gamma^\delta)\delta^{\beta\delta}h_M^\delta + |\Delta\gamma^\delta|\frac{\partial h_M^\delta}{\partial \Delta\gamma^\beta}\right]\right\}$$
$$+ \sum_\delta \left\{[q_\Omega + (1 - q_\Omega)\delta^{\alpha\delta}]\left[\text{sign}(\Delta\gamma^\delta)\delta^{\beta\delta}h_\Omega^\delta + |\Delta\gamma^\delta|\frac{\partial h_\Omega^\delta}{\partial \Delta\gamma^\beta}\right]\right\}, \tag{42}$$

where

$$\frac{\partial h_M^\delta}{\partial \Delta\gamma^\beta} = c_M\text{sign}(\Delta\gamma^\beta)\left(\frac{c_M\gamma}{b_M\tau_M^o} + 1\right)^{b_M - 1}, \tag{43}$$

$$\frac{\partial h_\Omega^\alpha}{\partial \Delta\gamma^\beta} = \frac{1}{f}\sum_\pi f^\pi \frac{\partial h_\Omega^{\pi^\alpha}}{\partial \Delta\gamma^\beta}\sqrt{(\widetilde{\mathbf{s}}^\alpha \otimes \widetilde{\mathbf{m}}^\alpha)_S \cdot \widetilde{\mathbf{H}}^\pi(\widetilde{\mathbf{s}}^\alpha \otimes \widetilde{\mathbf{m}}^\alpha)_S}, \tag{44}$$

$$\frac{\partial h_\Omega^{\pi^\alpha}}{\partial \Delta\gamma^\beta} = -2\frac{h_\Omega^{o^2}\text{sign}(\Delta\gamma^\beta)}{\tau_\Omega^s - \tau_\Omega^o}\text{sech}^2\frac{h_\Omega^o\gamma}{\tau_\Omega^s - \tau_\Omega^o}\tanh\frac{h_\Omega^o\gamma}{\tau_\Omega^s - \tau_\Omega^o}. \tag{45}$$

The dependence of $\widetilde{\mathbf{H}}^\pi$ on $\Delta\gamma^\alpha$ through rotation of $\widetilde{\mathbf{e}}_i^\pi$ is assumed negligible in this derivation. However, $\widetilde{\mathbf{H}}^\pi$ is updated at the end of each Newton iteration, with respect to precipitate rotations.

Applying approximations $\mathbf{f}_p = \mathbf{1} + \sum_{\alpha\in A}\Delta\gamma^\alpha \widetilde{\mathbf{s}}^\alpha \otimes \widetilde{\mathbf{m}}^\alpha$ and $\frac{1}{1 + b_x|\Delta\gamma|} \approx 1 - b_x|\Delta\gamma|$, while neglecting higher order terms in the resolved shear strains $\Delta\gamma^\alpha$, the back stress given in (35) can be reformulated as

$$\widetilde{\mathbf{X}} = (1 - b|\Delta\gamma|)\widetilde{\mathbf{X}}^n + 2(\widetilde{\mathbf{X}}^n\sum_\alpha \Delta\gamma^\alpha \widetilde{\mathbf{s}}^\alpha \otimes \widetilde{\mathbf{m}}^\alpha)_s + c_x f\widetilde{\boldsymbol{\Gamma}}_e\widetilde{\mathbf{H}}\sum_\alpha \Delta\gamma^\alpha(\widetilde{\mathbf{s}}^\alpha \otimes \widetilde{\mathbf{m}}^\alpha)_S + \text{O}(\Delta\gamma^{\alpha^2}).$$

The linearization yields $\frac{\partial \widetilde{\mathbf{X}}}{\partial \Delta\gamma^\beta} \approx 2(\widetilde{\mathbf{X}}^n\widetilde{\mathbf{s}}^\beta \otimes \widetilde{\mathbf{m}}^\beta)_s - b_x\text{sign}(\Delta\gamma^\beta)\widetilde{\mathbf{X}}^n + c_x f\widetilde{\boldsymbol{\Gamma}}_e\widetilde{\mathbf{H}}(\widetilde{\mathbf{s}}^\beta \otimes \widetilde{\mathbf{m}}^\beta)_s$ and considering $\frac{\partial x^\alpha}{\partial \Delta\gamma^\beta} \approx (\widetilde{\mathbf{s}}^\alpha \otimes \widetilde{\mathbf{m}}^\alpha)_s \cdot \frac{\partial \widetilde{\mathbf{X}}}{\partial \Delta\gamma^\beta}$ we obtain

$$\frac{\partial x^\alpha}{\partial \Delta\gamma^\beta} \approx (\widetilde{\mathbf{s}}^\alpha \otimes \widetilde{\mathbf{m}}^\alpha)_s \cdot (2(\widetilde{\mathbf{X}}^n\widetilde{\mathbf{s}}^\beta \otimes \widetilde{\mathbf{m}}^\beta)_s - b_x\text{sign}(\Delta\gamma^\beta)\widetilde{\mathbf{X}}^n + c_x f\widetilde{\boldsymbol{\Gamma}}_e\widetilde{\mathbf{H}}(\widetilde{\mathbf{s}}^\beta \otimes \widetilde{\mathbf{m}}^\beta)_s). \tag{46}$$

It should be noted that in case of multiple slip deformation, the active slip system sets determined by the algorithmic treatment outlined in Appendix A may not be unique and different sets can be obtained depending on the initial/trial active set at the beginning of the time step. A schematic summary of the stress integration procedure is given in Table A of Appendix A. Also, under particular hardening situations, some of the slip systems in the determined sets may be redundant and the Jacobian matrix $[D^{\alpha\beta}]$ can be

ill-conditioned or singular. Numerical treatments for such cases have been suggested by Miehe and Schrö-der (2001) and applied to back stress formulations in Han et al. (2004b) which has been summarized in Appendix B for convenience of the reader.

5. Numerical examples

Most of experimental investigations on the hardening of crystals are limited to simple tension tests (e.g., Chang and Asaro, 1981). Although several references can also be found on experimentally determined Bauschinger effects and transient deformation such as Khan and Cheng (1998) on copper crystals and Edwards and Washborn (1954) on zinc crystals, experimental data on back stresses and Bauschinger effects in precipitated crystals seem unavailable. The quantitative comparison of the proposed material model and simulation procedure with experimental data is, therefore, rather difficult so that the main aim of the following examples is to qualitatively illustrate the behavior of the suggested model. Particular interest is addressed to the effect of the particle description $\widetilde{\mathbf{H}}$ on the anisotropic hardening behavior at moderate to large strains. The numerical algorithm described in the previous sections has been implemented into the ABAQUS explicit (2002) material user interface and all simulations have been performed explicitly. The step sizes have been chosen in such a way that the kinetic energy is negligible compared to the strain energy. For completeness and later use, the applied order of the twelve slip systems of a FCC crystal has been given in Table 3. For simplicity, the initial critical resolved shear stressed τ_{Mo}^{α} are assumed to be the same for all slip systems and the material parameters $s_{\Omega o}^{\pi}$ are assumed to be the same for all precipitates. The material parameters applied in the following examples are given in Table 4 if not otherwise noted in the text.

5.1. Initial yield

To illustrate the plastic anisotropy in the initial yield of the suggested model, tensile deformation of Al–xCu crystals with different microstructures are considered. The microstructure is usually controlled by aging processes. The resulting microstructures were correlated with the yield stress and analyzed with respect to continuum mechanics models and computer simulations in Zhu et al. (2000). The yield stresses

Table 3
Slip directions $\mathbf{s}^{\alpha}$ and planes $\mathbf{m}^{\alpha}$ of the slip systems α in Miller indices notation

α	$\mathbf{s}^{\alpha}$	$\mathbf{m}^{\alpha}$	α	$\mathbf{s}^{\alpha}$	$\mathbf{m}^{\alpha}$	α	$\mathbf{s}^{\alpha}$	$\mathbf{m}^{\alpha}$	α	$\mathbf{s}^{\alpha}$	$\mathbf{m}^{\alpha}$
1	[011]	(11$\bar{1}$)	4	[01$\bar{1}$]	(1$\bar{1}\bar{1}$)	7	[011]	(11$\bar{1}$)	10	[011]	(11$\bar{1}$)
2	[101]	(11$\bar{1}$)	5	[101]	(1$\bar{1}\bar{1}$)	8	[10$\bar{1}$]	(11$\bar{1}$)	11	[10$\bar{1}$]	(11$\bar{1}$)
3	[1$\bar{1}$0]	(11$\bar{1}$)	6	[110]	(1$\bar{1}\bar{1}$)	9	[011]	(11$\bar{1}$)	12	[011]	(11$\bar{1}$)

Table 4
Material parameters of the Al–Cu single crystal

Young's modulus $E = 70{,}000$ MPa	$q_{\Omega} = 1.4$
Poisson's ratio $v = 0.3$	$h_{\Omega}^{o} = 135$ MPa
$q_M = 1.4$	$\tau_{\Omega}^{o} = 60$ MPa
$\tau_M^o = 0.98$ MPa	$\tau_{\Omega}^{S} = 100$ MPa
$b_M = 0.4$	$b_x = 30.0$
$c_M = 784$ MPa	$c = 2.0$
$\tau_{Mo}^{\alpha} = 10$ MPa	$s_{\Omega o}^{\pi} = 50$ MPa
$f = 0.03$[a]	

[a] This value is used for all the simulations unless otherwise noted as for Tables 5–7.

of the stress-aged specimens were found to be lower than those of the stress-free-aged specimens, either when the test direction was along or perpendicular to the aging-stress direction. This was attributed to the effect of stress-induced preferential orientation of the $\theta'\{1\,0\,0\}$-plates as well as to their different volume fraction and/or morphology in the stress-aged specimen subjected to the same thermal treatment as the stress-free-aged specimen. It should be noted that for stress-aged specimens, precipitates preferentially form perpendicular to the compressive aging-stress direction.

Table 5
Quantitative TEM analysis data of θ'-platelet precipitates in the Al–Cu specimens subjected to compression tests (from Zhu et al., 2000)

Specimen number[a]	Test angle θ[b]	Volume fraction[c]	Alignment ratio ($\|$:$\perp$)[d]
1f	0°	0.0229	50:50
1s	0°	0.0215	100:0
2f	0°	0.0227	50:50
2s	0°	0.0197	98:2
3f	0°	0.0216	50:50
3s	0°	0.0199	99:1
4f	0°	0.0195	50:50
4s	0°	0.0199	98:2
5f	0°	0.0177	50:50
5s	0°	0.0171	98:2
9f	90°	0.0165	49:51
9s	90°	0.0156	99:1

[a] f and s denote stress-free and stress-aged, respectively.
[b] Angle between directions of mechanical tests and stress application during stress aging (with 0°, the mechanical test direction is [1 0 0] and with 90°, the mechanical test direction is [0 1 0]).
[c] Volume fraction of the θ'-plates measured by quantitative TEM.
[d] The number ratio of the plates whose normal directions are parallel to the applied aging-stress direction to those perpendicular.

Table 6
Comparison between experimental and simulation results for the modified axial component of the initial yield stress, τ_{axial} in the stress-free-aged and stress-aged Al–Cu specimens

Specimen number[a]	Experimental tests		Simulation results			
	τ_{axial}^{ex} (MPa)[b]	δ^{ex} (%)[c]	τ_{axial} (MPa)	δ (%)	Hosford et al. δ^H(%)[d]	Bate et al. δ^B (%)[e]
1f	80	−15.3	77.5	−7.9	−6.1	−33.6
1s	67.8		71.3			
2f	78	−13.1	77.3	−7.7	−17.1	−26.5
2s	67.8		71.4			
3f	79.2	−12.4	77.3	−7.7	−7.9	−31.9
3s	69.4		71.4			
4f	68.6	−12.0	77.2	−7.5	2.1	−41.8
4s	60.4		71.4			
5f	67.8	−22.3	77.1	−7.4	−3.4	−36.4
5s	52.7		71.4			
9f	63.7	−3.9	76.7	−3.6	1.2	21.9
9s	61.2		73.9			

[a] f and s denote stress-free and stress-aged, respectively.
[b,c,d,e] Data from Zhu et al. (2000).
[b] Strengthening stress $\tau_{axial} = (\sigma - \sigma_0) \times \eta$ is the contribution to the initial yield stress due to Cu solid solution hardening, where η is the Schmid factor for the single crystal, and σ is the measured initial yield stress. The value of σ_0 is set to 55 MPa and η to 1/2.45.
[c] δ is the difference between the stresses τ_{axial} of stress-free-aged and stress-aged specimens, i.e. $\delta = -100 \times (\tau_{axial,f} - \tau_{axial,s})/\tau_{axial,f}$.

The quantitative TEM analysis of the θ'-plates in the Al–Cu specimens and the simple compression tests given in Zhu et al. (2000) are summarized in Table 5, where the compressive aging-stress direction is aligned with the $[1\,0\,0]$ direction in the single crystal. The compressive mechanical test direction is aligned with the $[1\,0\,0]$ direction in the single crystal for the 0° test angle and $[0\,1\,0]$ for the 90° test angle, respectively. To illustrate the performance of the proposed approach, numerical calculations have been preformed and results in the initial yield stress (calculated/modified axial components of the initial yield stress, τ_{axial} which represents the contribution of precipitates to the initial yield stress) were compared with experimental results obtained by Zhu et al. (2000) and predictions listed therein obtained by the models suggested in Hosford and Zeisloft (1972) and Bate et al. (1981). For these simulations, each volume fraction of precipitates whose normal directions are parallel to the applied $[1\,0\,0]$ aging-stress direction is calculated by considering both the overall volume fraction of precipitates and the ratio of the plates whose normal directions are parallel to the applied aging-stress direction to those perpendicular to it. In Table 6 the calculated axial components of the initial yield stress τ_{axial} are compared with experimental results and predictions of the models by Hosford and Zeisloft (1972) and Bate et al. (1981). In this comparison, the experimental axial component of the initial yield stress is obtained by $\tau_{axial} = (\sigma - \sigma_0) \times \eta$, where σ is the measured axial initial yield stress with precipitates, σ_0 is the contribution of Cu solid solution hardening to the initial yield stress and η is the Schmid factor. As in Zhu et al. (2000) the relative difference δ between the strengthening stress $\tau_{axial,f}$ of the stress-free-aged specimen and $\tau_{axial,s}$ of the stress-aged specimen has been applied as comparison in Table 6 and the predictions of the suggested model τ_{axial} are qualitatively in accordance with the experiments τ_{axial}^{ex}, in as far as the stresses of the stress-aged specimens are lower than those of the stress-free aged specimens, whether or not the test direction was along or perpendicular to the aging-stress direction. In addition our proposed model yields closer results to those obtained experimentally than the models of Hosford and Zeisloft (1972) and Bate et al. (1981).

5.2. Monotonous loading

The performance of the suggested model in the hardening behavior for monotonous loading will be discussed next by considering tensile compression tests. As in Cuitino and Ortiz (1992) and Anand and Kothari (1996), simulations are performed using a single eight-node continuum element under
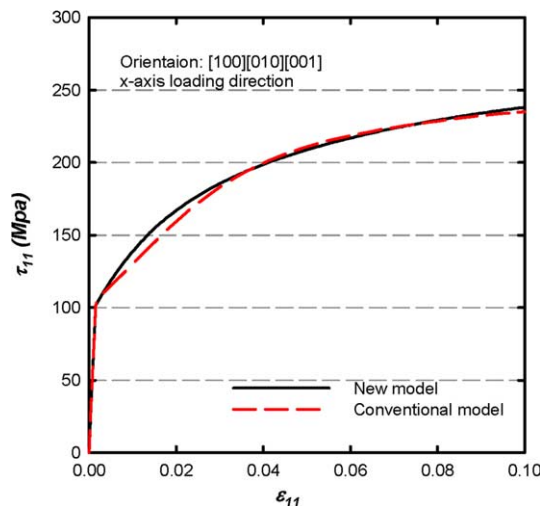

Fig. 5. τ_{11} versus ε_{11} in $[1\,0\,0]$ orientation without (conventional model) and with precipitates (new model).
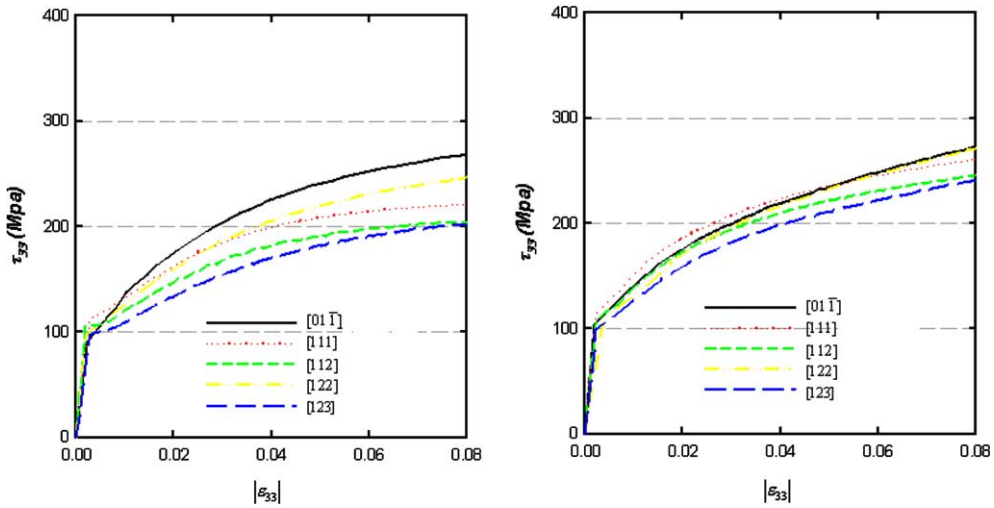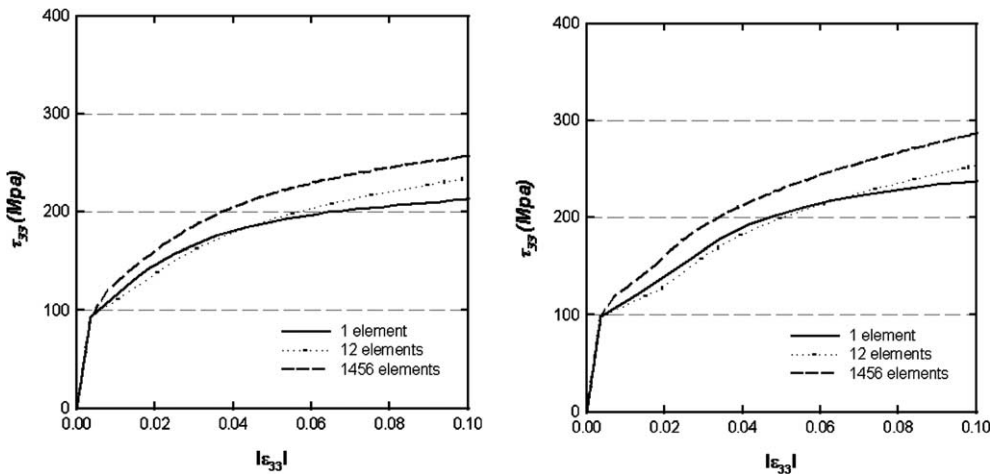
homogeneous deformation. Simple stretch directions are aligned to the element edges and all faces remain parallel to the initial configuration. A volume fraction of $f = 0.03$ and a equally distribution of the precip-

Table 7
Material parameters for the conventional model[a]

g_0^α	q	h_0	τ_s	τ_0
41 MPa	1.4	600 MPa	104 MPa	60 MPa

[a] Model of Chang and Asaro (1981): slip resistance $\dot{g}^\alpha = \sum_\beta h_g^{\alpha\beta} |\dot{\gamma}^\beta|$, $h_g^{\alpha\beta} = [q + (1-q)\delta^{\alpha\beta}] h_g^\beta$ and $h_g^\beta = h_0 \operatorname{sech}^2\left(\frac{h_0\gamma}{\tau_s - \tau_0}\right)$.

Fig. 6. τ_{33} versus $|\varepsilon_{33}|$ in various orientations without (left) and with (right) precipitates.

Fig. 7. Cylinder compression in [1 2 2] direction, averaged τ_{33} versus $|\varepsilon_{33}|$ for 1, 12 and 1456 finite elements without (left) and with (right) precipitates.

itates along the habit planes $[1\,0\,0]$, $[0\,1\,0]$ and $[0\,0\,1]$ is assumed. For comparison additional simulations with a conventional hardening model, e.g., Chang and Asaro (1981), have been performed where the precipitate substructure is not taken into account. Material parameters of this conventional model are fitted in such a way that the stress–strain behavior in $[1\,0\,0]\,[0\,1\,0]\,[0\,0\,1]$ orientation of both models have a similar behavior (see Fig. 5). The determining material parameters of the conventional model, as explained above, are listed in Table 7. In Fig. 6 the compressive stresses over the compressive strain in various crystalline orientations are illustrated where the anisotropy of the hardening behavior is reduced in the predictions of the suggested material model considering the precipitate substructure. In this respect it should be noted that in comparison to pure Al-crystals, a reduced anisotropic hardening behavior was reported in experiments for alloys containing θ' precipitates (Hosford and Zeisloft, 1972).

In the above considerations homogeneous deformation was assumed which may not be present in experimental tests. Even for simple compression tests, local lattice rotations from boundary constraints arise yielding inhomogeneous deformation. As a result, a homogeneous single crystal can transform into a multi-crystal at higher strains. Therefore, simulations of experimental tests have to be performed with more than one element to capture the real deformation process.
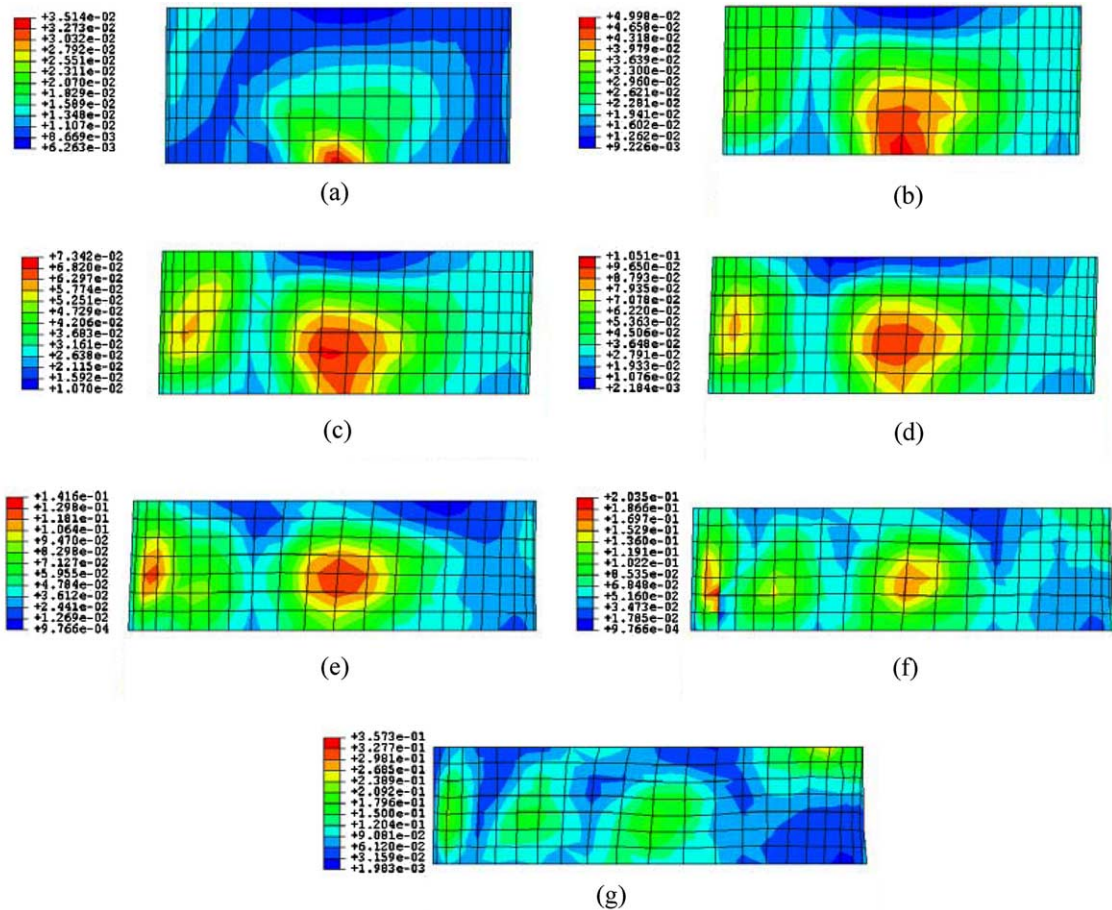

Fig. 8. Lattice rotation (in radians) from the compressive axis at different ε_{33} for orientation $[1\,2\,2]\,[2\,\bar{1}\,0]\,[2\,4\,\bar{5}]$: (a) $\varepsilon_{33} = -0.05$, (b) $\varepsilon_{33} = -0.1$, (c) $\varepsilon_{33} = -0.15$, (d) $\varepsilon_{33} = -0.2$, (e) $\varepsilon_{33} = -0.25$, (f) $\varepsilon_{33} = -0.3$, (g) $\varepsilon_{33} = -0.35$.

As an example, a circular cylinder with radius 5 mm and height 5 mm is considered. The bottom plane is fixed in vertical z-direction and the top plane is moved down for the simple compression test case. Fig. 7 shows averaged compressive stresses over averaged compressive strain with 1, 12 and 1456 elements in direction [1 2 2] with differences in the order of 25%. Finer discretizations than the 1456 elements yielded practically identical results and, therefore, the results in the stress can be considered to be converged with respect to mesh refinements. A remarkable stress decrease has been computed at $\varepsilon_{33} = -0.15$ in the case of 1456 elements. Such decreases have been observed and discussed by Asaro (1978), Rashid and Nemat-Nasser (1992) and Miehe (1996) and these stress-decreasing phenomena are caused by local lattice rotations into softer orientations.

To illustrate the inhomogeneous deformation, in Figs. 8 and 9 the contours of the lattice rotation (in radians) to the compressive axis and {1 1 1} pole figures according to the corresponding compressive
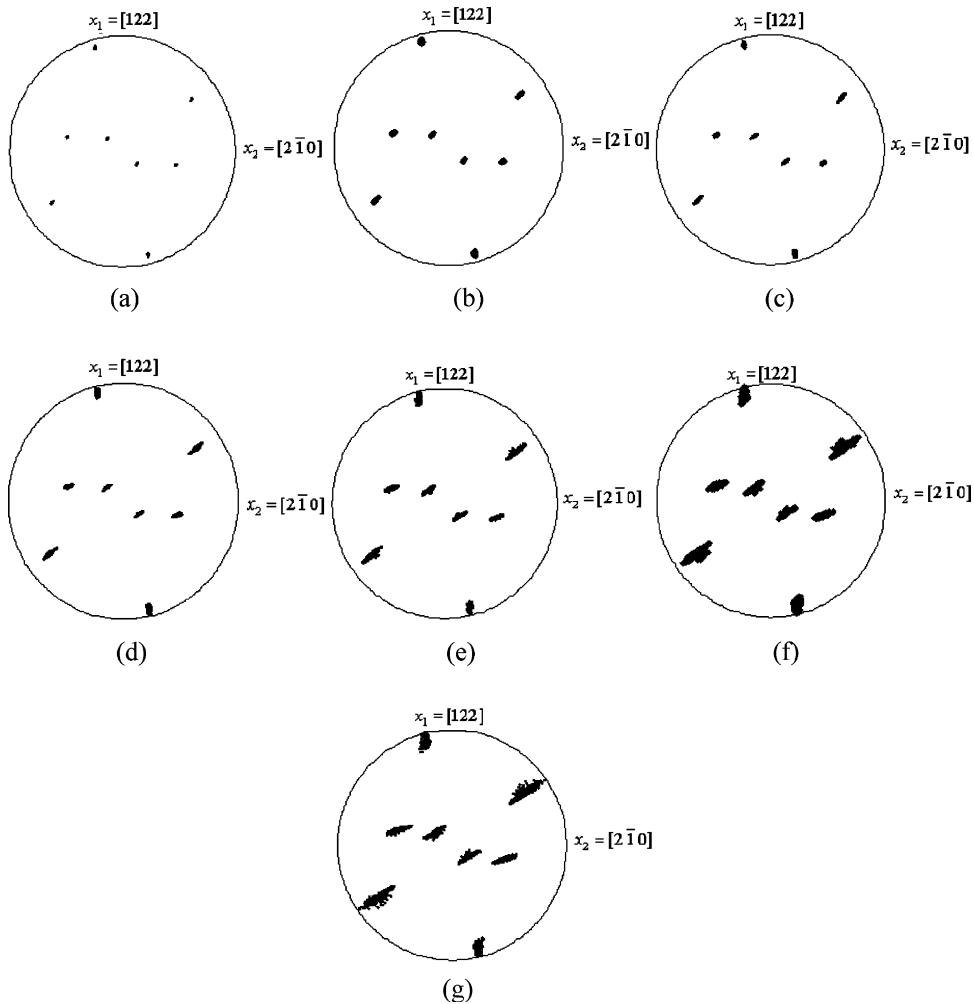

Fig. 9. {1 1 1} pole figures* compressed cylinder in $[1\,2\,2]\,[2\,\bar{1}\,0]\,[2\,4\,\bar{5}]$ orientation at different strains. [*8 slip normal directions are plotted here, i.e., $(1\,1\,1)$, $(\bar{1}\,1\,1)$, $(1\,\bar{1}\,1)$, $(1\,1\,\bar{1})$, $(\bar{1}\,\bar{1}\,1)$, $(\bar{1}\,1\,\bar{1})$, $(1\,\bar{1}\,\bar{1})$ and $(\bar{1}\,\bar{1}\,\bar{1})$]: (a) $\varepsilon_{33} = -0.05$, (b) $\varepsilon_{33} = -0.1$, (c) $\varepsilon_{33} = -0.15$, (d) $\varepsilon_{33} = -0.2$, (e) $\varepsilon_{33} = -0.25$, (f) $\varepsilon_{33} = -0.3$, (g) $\varepsilon_{33} = -0.35$.

logarithmic strain ε_{33} for the $[1\,2\,2]$ $[2\,\bar{1}\,0]$ $[2\,4\,\bar{5}]$ crystalline orientation are given, respectively. Local lattice rotations yield inhomogeneous deformation, since the material at the top and bottom can not rotate as in
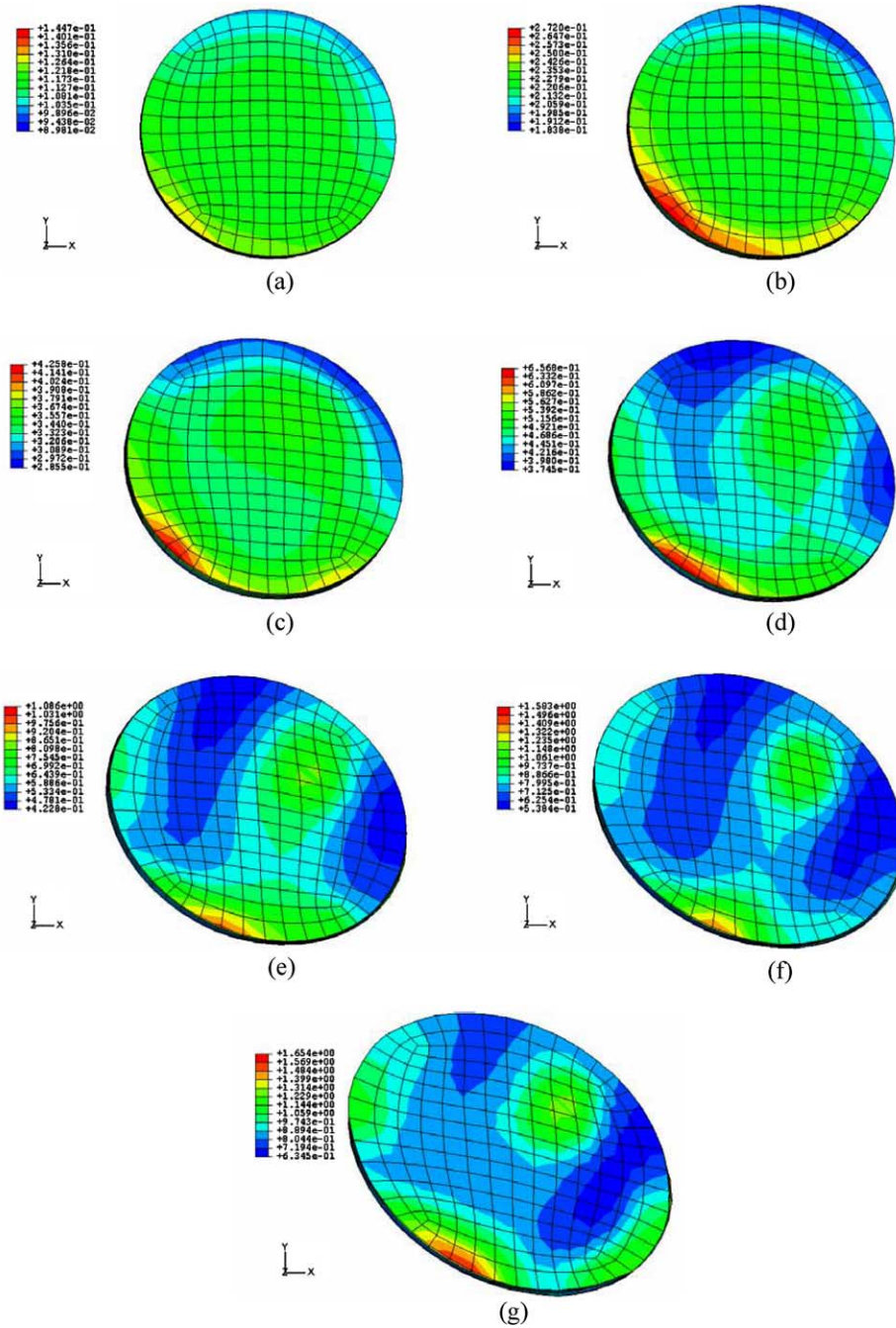

Fig. 10. Accumulated shear strain γ versus ε_{33}: (a) $\varepsilon_{33} = -0.05$, (b) $\varepsilon_{33} = -0.1$, (c) $\varepsilon_{33} = -0.15$, (d) $\varepsilon_{33} = -0.2$, (e) $\varepsilon_{33} = -0.25$, (f) $\varepsilon_{33} = -0.3$, (g) $\varepsilon_{33} = -0.35$.

the interior. The inhomogeneity is also illustrated in Fig. 10 where the equivalent plastic strain is plotted for different compressive strains ε_{33}. The inhomogeneity increases with the deformation, which can be seen by the minimum and maximum values of the equivalent plastic strain, starting with min/max strains of 0.08981 and 0.1447 at $\varepsilon_{33} = -0.05$ to 0.6345 and 1.654 at $\varepsilon_{33} = -0.35$. As a consequence, the orientation of the single crystal can be considered to change locally, as it has been also observed experimentally and numerically in Becker et al. (1991).

In order to assess the transversal anisotropy with an initially circular cross-section for the cases without (Chang and Asaro, 1981) and with precipitates (suggested model), distances of four marked points are plotted during the deformation process in Fig. 11. For the case with precipitates, the length difference between the major and minor axis is smaller than for the case without precipitates. This indicates that the predicted anisotropy by the suggested model is reduced in comparison to the conventional model where the precipitate structure is not reflected.

5.3. Back stress and non-monotonous loading

While Bauschinger effects are known to be not rather small for single phased aluminum, materials with precipitates are known to exhibit strong Bauschinger effects (e.g., Bate et al., 1982) which are accounted for by back stresses in the material description. In Fig. 12 strains versus stresses in tension-compression in different directions are illustrated, showing the differences in kinematic hardening. Up to 5% strain, the hardening is not significantly affected by the precipitate rotation with relative to the lattice as shown in Fig. 4. The strong increase in the flow stress is related to both kinematic and isotropic hardening. At larger strains of more than 0.05 strain the differences become more significant as can be seen from the tension curves in Fig. 13 where the strains versus total stress is shown in comparison with the back stress. Fig. 14 shows stress–strain diagrams where the material is first deformed in x_1-direction and than in the x_2-direction. While the $[1\,1\,0]\,[0\,0\,1]\,[1\,\bar{1}\,0]$ orientation is hardly affected by the precipitate rotation the $[1\,2\,2]\,[2\,\bar{1}\,0]\,[2\,4\,\bar{5}]$ orientation shows quite considerable differences in the hardening behavior applying the precipitate rotation or not.
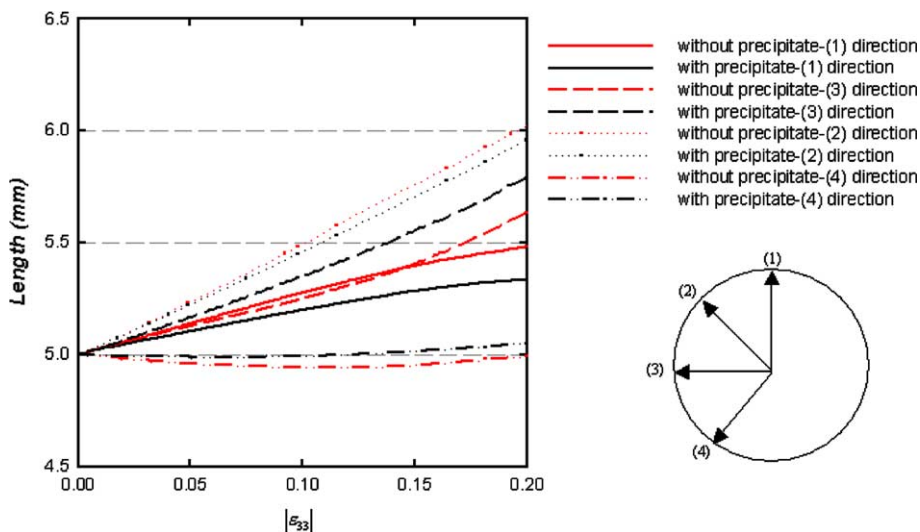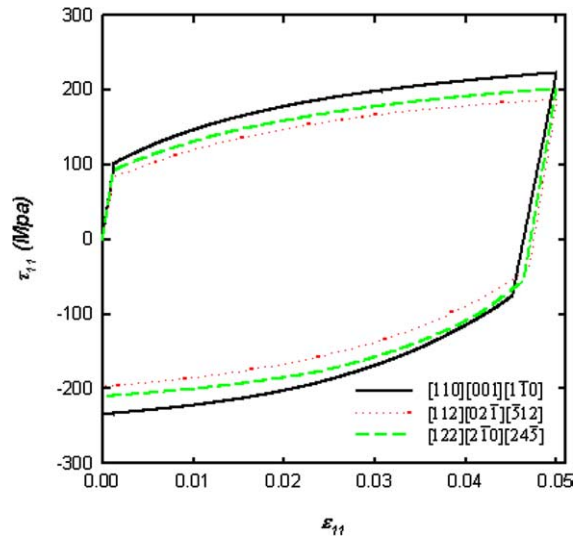

Fig. 11. Distance changes during deformation.

Fig. 12. Tensile and reverse stresses (τ_{11}) versus ε_{11} in [1 1 0], [1 1 2] and [1 2 2] direction.
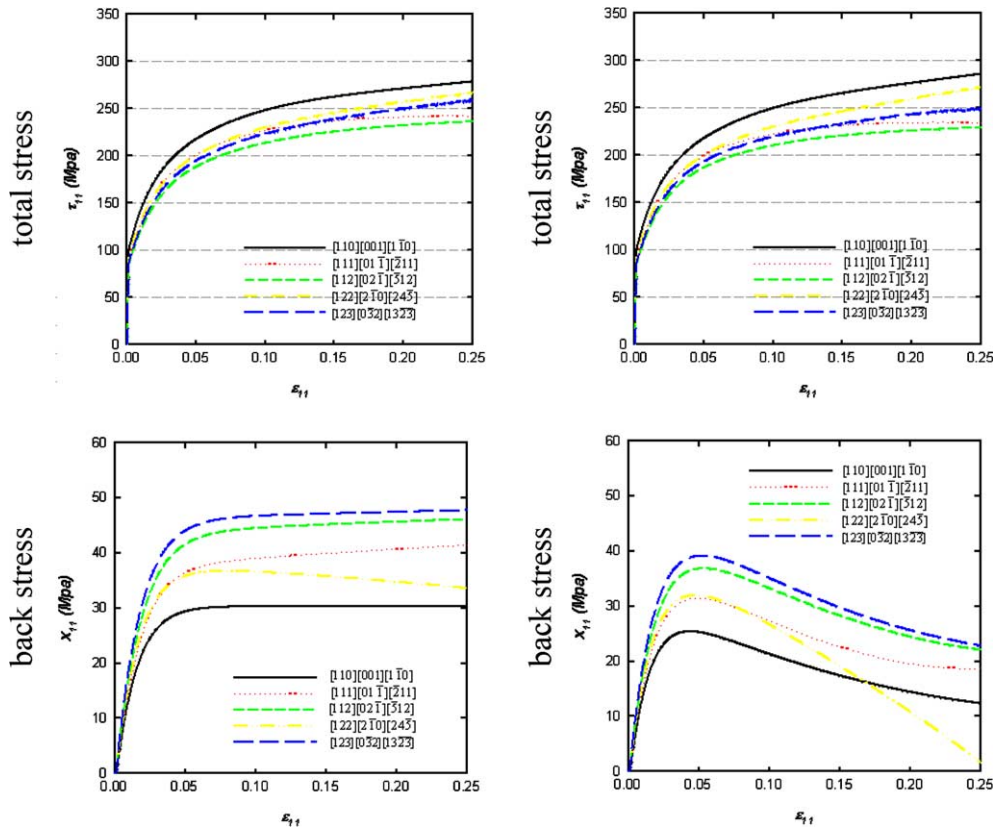

Fig. 13. Stress components τ_{11} (top) and x_{11} (below) over ε_{11} in various orientations without (left) and with (right) precipitate rotation.
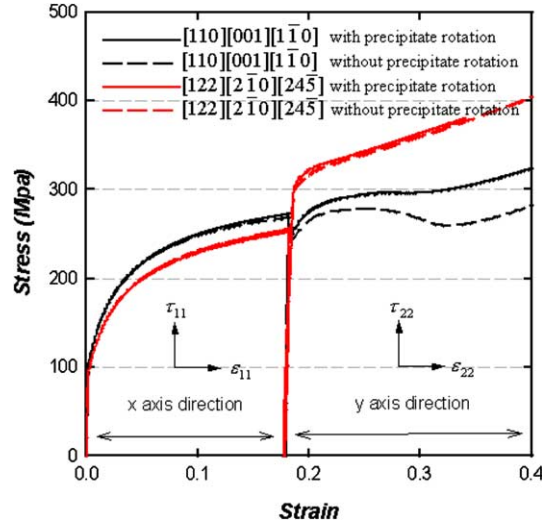
Fig. 14. Stress–strain curves (τ_{11}–ε_{11} and τ_{22}–ε_{22}) in $[1\,1\,0]\,[0\,0\,1]\,[1\,\bar{1}\,0]$ and $[1\,2\,2]\,[2\,\bar{1}\,0]\,[2\,4\,\bar{5}]$ crystalline orientations with load path change.

6. Conclusions

The effect of the thin precipitates on the anisotropy of the initial slip resistance and isotropic-kinematic hardening has been modeled in this article and a corresponding elastic–plastic rate independent algorithmic treatment has been derived. From the results of the numerical simulation it is found that the suggested model represents the initial plastic anisotropy at least qualitatively well and that it has an improved representation of various characteristic hardening behaviors in comparison with conventional hardening descriptions where the precipitate structure is not reflected.

Acknowledgement

Appendix A. Determination of the active slip systems

The Newton iteration outlined in Section 4 to determine the plastic slip is embedded into the following iterative procedure for the determination of the active set of slip systems A, which enforces the Kuhn–Tucker type loading and unloading conditions, thus $\mathrm{sign}(\tau^\alpha - x^\alpha)\Delta\gamma^\alpha \geqslant 0$ and $\Phi^\alpha \leqslant 0$ for all $\alpha \in A$. At the beginning of the iteration, a first estimate $A = A_n$ is assumed, thus the trial active set at time t_{n+1} coincides with the one at time t_n. If the results obtained by the Newton iteration contradict constraints $(15)_1$ and $(15)_2$, the Newton iteration is restarted with $A = \{\alpha\}$ of the maximal violated Φ^α. Other slip systems are then added or removed successively one after the other. Each single change of the active set is accompanied by the Newton iteration for the incremental slip. After consistency has been restored by the Newton iteration, conditions $(15)_1$ and $(15)_2$ are checked again. If some parameters $\Delta\gamma^\alpha$ in $\alpha \in A$ violate the discrete loading condition

Table A
Stress integration scheme

Variable input: $\mathbf{F}$, $\mathbf{F}_p^n$, γ^α, g^{α^n}, $\widetilde{\mathbf{X}}^n$, A_n

(E) Elastic predictor:

    Compute: $\widetilde{\mathbf{S}}^{\text{trial}}$, $\tau^{\alpha^{\text{trial}}}$, $\tau^{\alpha^{\text{trial}}}$, $\tau^{\alpha^{\text{trial}}}$

    If $\Phi^{\alpha^{\text{trial}}} \leqslant 0$ for all $\alpha \in S$ then

      $\mathbf{F}_p^{n+1} = \mathbf{F}_p^n$, $\gamma^{n+1} = \gamma^n$, $g^{\alpha^{n+1}} = g^{\alpha^n}$, $\widetilde{\mathbf{X}}^{n+1} = \widetilde{\mathbf{X}}^n$, $\widetilde{\mathbf{S}}^{n+1} = \widetilde{\mathbf{S}}^{\text{trial}}$, $A_{n+1} = \downarrow$

    and Exit

(P) Plastic predictor:

    Initialize active set iteration counter $i_{\text{set}} = 0$ and set $A_{n+1} = A_n$

    (A) determination of the active slip systems:

      □ $i_{\text{set}} = i_{\text{set}} + 1$

        If ($i_{\text{set}} = 2$ and $A_{n+1} \neq \downarrow$) then set $A_{n+1} = \{\alpha = \arg[\max \Phi^\alpha] \in S\}$

      □ $\Delta\gamma^\alpha = 0$ for all $\alpha \in S$ and $k = 0$

     (N) Newton iteration:

       ○ $k = k + 1$

       ○ Compute $D^{\alpha\beta^k}$ for $\alpha, \beta \in A$

       ○ If needed regularize $D^{\alpha\beta^k}$ via (47) and (48)

       ○ $\Delta\gamma^{\alpha^{k+1}} = \Delta\gamma^{\alpha^k} + \sum_\beta [D^{\alpha\beta^k}]^{-1} r^{\beta^k}$

       ○ $\gamma^{k+1} = \gamma^n + \sum_\alpha |\Delta\gamma^{\alpha^{k+1}}|$, update $\tilde{\mathbf{e}}_i^\pi$ and $\widetilde{\mathbf{H}}$ via (23)

       ○ Compute $r^{\beta^{k+1}}$. If $\|\mathbf{r}^{k+1}\| \geqslant \text{tol}$ go to (N)

      □ If $\exists \alpha \in A$: $\text{sign}(\tau^\alpha - x^\alpha)\,\Delta\gamma^\alpha < 0$ then

        drop minimal loaded system, thus,

        $A = \{A/(\alpha = \arg[\min \Phi^\alpha] \in A)\}$ and go to (A)

      □ If $\exists \alpha \in A$: $\Phi^\alpha > 0$ then

        add maximal loaded system, thus,

        $A = \{A \cup (\alpha = \arg[\max \Phi^\alpha] \in S/A)\}$ and go to (A)

Variable output: $\mathbf{F}_p^{n+1}$, γ^{n+1}, g^{α^n}, $\widetilde{\mathbf{X}}^n$, $\widetilde{\mathbf{S}}^{n+1} = \widetilde{\mathbf{S}}^{\text{trial}}$, A_{n+1}

$\text{sign}(\tau^\alpha - x^\alpha)\Delta\gamma^\alpha \geqslant 0$, the minimal loaded system is removed from A and the local Newton iteration is re-started with $\Delta\gamma^\alpha \geqslant 0$ for all $\alpha \in A$.

Having obtained a converged solution of an active set with $\text{sign}(\tau^\alpha - x^\alpha)\Delta\gamma^\alpha \geqslant 0$ for all $\alpha \in A$, condition $\Phi^\alpha \leqslant 0$ is checked by monitoring the yield criteria of non-active systems S/A. For violations in some slip systems, the maximal loaded system of this set-not contained in A—is added and the Newton iteration is restarted. Otherwise, the local iteration is terminated. The whole stress integration procedure has been schematically summarized in Table A.

Appendix B. Numerical treatment for ill-conditioned Jacobian matrixes

Under particular loading situations, some slip systems in the determined sets may be redundant and the Jacobian matrix $[D^{\alpha\beta}]$ can be ill-conditioned or singular. Numerical treatments for such cases have been suggested by Anand and Kothari (1996) and Miehe and Schröder (2001). Here the regularization by the inverse based perturbation technique, proposed by Miehe and Schröder (2001), is adopted. For this, $[D^{\alpha\beta}]$ in (40) is factorized into a lower $[L^{\alpha\beta}]$, a upper tri-diagonal $[U^{\alpha\beta}]$, and a diagonal matrix $[d^{\alpha\beta}] = \text{diag}[d^1, d^2, \ldots, d^n]$ as $[D^{\alpha\beta}] = [L^{\alpha\beta}][d^{\alpha\beta}][U^{\alpha\beta}]$. If $|d^\alpha| < \varepsilon$ where $\varepsilon = c_{\min}\|\mathbf{D}\|_\infty$ is valid for one slip system α, then the diagonal terms of $[D^{\alpha\beta}]$ are modified via $D^{\alpha\alpha} \to D^{\alpha\alpha} + \text{sign}(D^{\alpha\alpha})\,\varepsilon$ to regularize the Jacobian matrix, where $c_{\min}$ denotes a given machine dependent minimum inverse condition number and norm $\|\cdot\|_\infty$ is defined by $\|\mathbf{D}\|_\infty = \max_\alpha \sum_\beta |D^{\alpha\beta}|$. This modified Jacobian is then used to solve (39).

References

ABAQUS, 2002. ABAQUS, Reference Manuals. Hibbit, Karlsson, Sorensen, Inc.

Abel, A., Ham, R.K., 1966. The cyclic strain behaviour of crystals of aluminum-4 wt.% copper—I. The Bauschinger effect. Acta Metall. 14, 1489–1494.

Anand, L., Kothari, M., 1996. A computational procedure for rate-dependent crystal plasticity. J. Mech. Phys. Solids 44, 525–558.

Asaro, R.J., 1978. Geometrical effects in the inhomogeneous deformation of ductile single crystal. Acta Metall. 27, 445–453.

Ashby, M.F., 1966. Work hardening of dispersion-hardened crystals. Phil. Mag. 14, 1157–1178.

Ashby, M.F., 1970. The deformation of plastically non-homogeneous materials. Phil. Mag. 21, 399–424.

Barlat, F., Liu, J., 1998. Precipitate-induced anisotropy in binary Al–Cu alloys. Mater. Sci. Eng. A 257, 47–61.

Barlat, F., Vasudevan, A.K., 1991. Influence of precipitate microstructure on flow and forming properties of an aluminum alloy sheet. Acta Metall. 39, 391–400.

Bate, P., Roberts, W.T., Wilson, D.V., 1981. The plastic anisotropy of two-phase aluminum alloys–I. Anisotropy in unidirectional deformation. Acta Metall. 29, 1797–1814.

Bate, P., Roberts, W.T., Wilson, D.V., 1982. The plastic anisotropy of two-phase aluminum alloys—II. Anisotropic behaviour in load-reversal tests. Acta Metall. 30, 725–737.

Beaudoin, A.J., Dawson, P.R., Mathur, K.K., Kocks, U.F., Korzekwa, D.A., 1994. Application of polycrystalline plasticity to sheet forming. Comput. Meth. Appl. Mech. Eng. 117, 49–70.

Becker, R., Butler, J.F., Hu, H., Lalli, L.A., 1991. Analysis of an aluminum single-crystal with unstable initial orientation (0 0 1) [1 1 0] in channel die compression. Metal. Trans. A 22, 45–58.

Brown, L.M., 1973. Back stress, image stress, and work-hardening. Acta Metall. 21, 879.

Brown, L.M., Stobbs, W.M., 1971a. The work hardening of copper-silica I. A model based on internal stresses, with no plastic relaxation. Phil. Mag. 23, 1185–1199.

Brown, L.M., Stobbs, W.M., 1971b. The work hardening of copper-silica II. The role of plastic relaxation. Phil. Mag. 23, 1201–1233.

Chang, Y.W., Asaro, R.J., 1981. An experimental study of shear localization in aluminum-copper single crystals. Acta Metall. 29, 241–257.

Clayton, J.D., McDowell, D.L., 2003. A multiscale multiplicative decomposition for elasto-plasticity of polycrystals. Int. J. Plast. 19, 1401–1444.

Cuitino, A.M., Ortiz, M., 1992. Computational modelling of single crystals. Modell. Simulat. Mater. Sci. Eng. 1, 225–263.

Edwards, E.H., Washborn, J., 1954. Strain hardening of latent slip systems in zinc crystals. Trans. AIME 200, 1229.

Engler, O., Kong, X.W., Lucke, K., 2001. Influence of precipitates on the microstructure and texture during the rolling of Al–Cu and Al–Mn single crystals with rolling texture orientations. Philos. Mag. A 81, 543–570.

Evers, L.P., Brekelmans, W.A.M., Geers, M.G.D., 2004. Scale dependent crystal plasticity framework with dislocation density and grain boundary effects. Int. J. Solids Struct. 41, 5209–5230.

Evers, L.P., Parks, D.M., Brekelmans, W.A.M., Geers, M.G.D., 2002. Crystal plasticity model with enhanced hardening by geometrically necessary dislocation accumulation. J. Mech. Phys. Solids 50, 2403–2424.

Han, C.-S., Gao, H., Huang, Y., Nix, W.D., 2005a. Mechanism-based strain gradient crystal plasticity—I. Theory. J. Mech. Phys. Solids 53, 1188–1203.

Han, C.-S., Gao, H., Huang, Y., Nix, W.D., 2005b. Mechanism-based strain gradient crystal plasticity—II. Analysis. J. Mech. Phys. Solids 53, 1204–1222.

Han, C.-S., Lee, M.-G., Chung, K., Wagoner, R.H., 2003. Integration algorithms for planar anisotropic shells with isotropic and kinematic hardening at finite strains. Commun. Numer. Meth. Eng. 19, 473–490.

Han, C.-S., Wagoner, R.H., Barlat, F., 2004a. On precipitate induced hardening in crystal plasticity: theory. Int. J. Plast. 20, 477–494.

Han, C.-S., Wagoner, R.H., Barlat, F., 2004b. On precipitate induced hardening in crystal plasticity: algorithms and simulations. Int. J. Plast. 20, 1441–1461.

Hosford, W.F., Zeisloft, R.H., 1972. The anisotropy of age-hardened Al-4 Pct Cu single crystals during plane-strain compression. Metall. Trans. 3, 113–121.

Humphreys, F.J., 1979. Local lattice rotations at second phase particles in deformed metals. Acta Metall. 27, 1801–1814.

Humphreys, F.J., Ardakani, M.G., 1994. The deformation of particle-containing aluminum single crystals. Acta Metall. Mater. 42, 749–761.

Kalidindi, S.R., Anand, L., 1992. Approximate procedure for predicting the evolution of crystallographic texture in bulk deformation processing of fcc metals. Int. J. Mech. Sci. 34, 309–329.

Khan, A.S., Cheng, P., 1998. Anisotropic elastic–plastic constitutive model for single and polycrystalline metals. II. Experiments and predictions concerning thin-walled tubular OFHC copper. Int. J. Plast. 14, 209–226.

Kim, H.-K., Oh, S.-I., 2003. Finite element analysis of grain-by-grain deformation by crystal plasticity with couple stress. Int. J. Plast. 19, 1245–1270.

Kiser, M.T., Zok, F.W., 1996. Plastic flow and fracture of a particulate metal matrix composite. Acta Mater. 44, 3465–3476.

Meissonnier, F.T., Busso, E.P., O'Dowd, N.P., 2001. Finite element implementation of a generalized non-local rate-dependent crystallographic formulation for finite strains. Int. J. Plast. 17, 601–640.

Miehe, C., 1996. Exponential map algorithm for stress updates in anisotropic multiplicative elastoplasticity for single crystals. Int. J. Numer. Meth. Eng. 50, 273–298.

Miehe, C., Schröder, J., 2001. A comparative study of stress update algorithms for rate-independent and rate-dependent crystal plasticity. Int. J. Numer. Meth. Eng. 50, 273–298.

Nouailhas, D., Cailletaud, G., 1995. Tension-torsion behavior of single-crystal superalloys, experiment and finite element analysis. Int. J. Plast. 11, 451–470.

Ohashi, T., 2004. Three dimensional structures of the geometrically necessary dislocations in matrix inclusion systems under uniaxial tensile loading. Int. J. Plast. 20, 1093–1109.

Oldroyd, J.G., 1950. On the formulation of rheological equations of state. Proc. Roy. Soc. Lond. A 200, 523–541.

Pierce, D., Asaro, R.J., Needleman, A., 1983. Material rate dependence and localized deformation in crystalline solids. Acta Metall. 31, 1951–1976.

Rashid, M.M., Nemat-Nasser, S., 1992. A constitutive algorithm for rate dependent crystal plasticity. Comput. Meth. Appl. Mech. Eng. 94, 201–228.

Schmitt, C., Lipinski, P., Berveiller, M., 1997. Micromechanical modelling of the elastoplastic behavior of polycrystals containing precipitates—application to hydro- and hyper-eutectoid steels. Int. J. Plast. 13, 183–199.

Shu, J.Y., 1998. Scale-dependent deformation of porous single crystals. Int. J. Plast. 14, 1085–1107.

Tanaka, K., Mori, T., 1970. The hardening of crystals by non-deforming particles and fibers. Acta Metall. 18, 931–941.

Zhou, Y., Neale, K.W., Toth, L.S., 1993. A modified model for simulating latent hardening during the plastic deformation of rate-dependent fcc polycrystals. Int. J. Plast. 9, 961–978.

Zhu, A.W., Chen, J., Starke Jr., E.A., 2000. Precipitation strengthening of stress-aged Al–xCu alloys. Acta Mater. 48, 2239–2246.